Monthly Notices of the ROYAL ASTRONOMICAL SOCIETY

MNRAS **498,** 2778–2797 (2020)
Advance Access publication 2020 August 19

doi:10.1093/mnras/staa2509

TFAW survey – I. Wavelet-based denoising of K2 light curves. Discovery and validation of two new Earth-sized planets in K2 campaign 1

D. del Ser [1,2,3]★ and O. Fors [1,2,3]

[1] *Departament de Física Quàntica i Astrofísica, Institut de Ciències del Cosmos (ICCUB), Universitat de Barcelona, IEEC-UB, Martí i Franquès 1, E-08028 Barcelona, Spain*
[2] *Observatori Fabra, Reial Acadèmia de Ciències i Arts de Barcelona, Rambla dels Estudis, 115, E-08002 Barcelona, Spain*
[3] *Department of Physics and Astronomy, University of North Carolina at Chapel Hill, Chapel Hill, NC 27599-3255, USA*

Accepted 2020 August 14. Received 2020 August 11; in original form 2020 April 3

ABSTRACT

The wavelet-based detrending and denoising method TFAW is applied for the first time to EVEREST 2.0-corrected light curves to further improve the photometric precision of almost all K2 observing campaigns (C1–C8, C12–C18). The performance of both methods is evaluated in terms of 6 h combined differential photometric precision (CDPP), simulated transit detection efficiency, and planet characterization in different SNR regimes. On average, TFAW median 6 h CDPP is ∼30 per cent better than the one achieved by EVEREST 2.0 for all observing campaigns. Using the transit least-squares (TLS) algorithm, we show that the transit detection efficiency for simulated Earth–Sun-like systems is ∼8.5× higher for TFAW-corrected light curves than that for EVEREST 2.0 ones. Using the light curves of two confirmed exoplanets, K2-44 b (high SNR) and K2-298 b (low SNR), we show that TFAW yields better Markov chain Monte Carlo posterior distributions, transit parameters compatible with the catalogued ones but with smaller uncertainties, and narrows the credibility intervals. We use the combination of TFAW's improved photometric precision and TLS enhancement of the signal detection efficiency for weak signals to search for new transit candidates in K2 observing campaign 1. We report the discovery of two new K2-C1 Earth-sized planets statistically validated, using the vespa software: EPIC 201170410.02, with a radius of $1.047^{+0.276}_{-0.257}R_\oplus$ planet orbiting an M-type star, and EPIC 201757695.02, with a radius of $0.908^{+0.059}_{-0.064}R_\oplus$ planet orbiting a K-type star. EPIC 201757695.02 is the 9th smallest planet ever discovered in K2-C1, and the 39th smallest in all K2 campaigns.

Key words: methods: data analysis – surveys – planets and satellites: detection – planets and satellites: fundamental parameters – planetary systems – stars: variables: general.

1 INTRODUCTION

Developed in the months following the failure of the second of the four reaction wheels of *Kepler*, the K2 mission (Howell et al. 2014) represented a new concept for *Kepler*'s operations given the spacecraft's ability to maintain pointing in all three axes with only two reaction wheels. This operation mode, which started in 2013 October and became fully operational in 2014 May, provided enough fuel to begin a series of 19 sequential campaigns observing a set of independent target fields distributed around the ecliptic plane. During this *Kepler* extended mission, among other community-proposed targets, late-type dwarf stars were favoured as targets due to the highest chance of detecting small planets lying in the habitable zone of their host stars. However, the failure of the reactions wheels degraded the photometric precision obtained for K2. Several decorrelation techniques were developed to improve the noise properties of the K2 light curves: pixel level decorrelation (PLD; Deming et al. 2015), K2P (Lund et al. 2015), K2SFF (Vanderburg & Johnson 2014), and EVEREST 2.0[1] (Luger et al. 2018). The latter, based on a PLD combined with a Gaussian process (GP) optimization, led to best photometric precision to date achieved with K2 light curves.

In many instances, the systematic variations in a given light curve are also shared by other stars and same data set. A common approach to remove those systematics is to identify the objects in the field that suffer from the same kind of variations as the target (e.g. correlated noise), and then apply a filter based on the light curves of those template stars. The Trend Filtering Algorithm (TFA; Kovács, Bakos & Noyes 2005) is often applied to remove systematic variations in ground-based time-domain surveys, in particular the ones searching exoplanetary transits and variable stars.

Optimizing the photometric precision achieved by an astronomical survey is a key factor to increase the probability of detecting periodic signals in the data. Here we apply TFAW (del Ser, Fors & Núñez 2018), the wavelet-based modification of TFA, to further improve the photometric precision achieved by the EVEREST 2.0 data. TFAW uses the wavelet transform's signal decoupling and denoising potential to estimate the noise contribution of the light curve and the shape of the underlying signal, and returns a denoised signal without modifying any of its intrinsic properties. We combine this improved photometric precision achieved by TFAW with the optimized detection of small planets obtained by the transit least-squares (TLS) algorithm (Hippke & Heller 2019) to

★ E-mail: danieldelser@gmail.com
[1] https://github.com/rodluger/everest

© 2020 The Author(s)
Published by Oxford University Press on behalf of the Royal Astronomical Society

Downloaded from https://academic.oup.com/mnras/article/498/2/2778/5894404 by guest on 10 November 2023

search for periodic signals, in particular, planetary transit ones, within the TFAW-corrected light curves.

In Section 2, we briefly describe the TFAW algorithm. In Section 3, we compare the TFAW performance, in terms of combined differential photometric precision (CDPP), with respect to the one obtained with the TFA and EVEREST 2.0 K2 data. We also evaluate the transit detection efficiency of Earth–Sun-like injected systems, in both EVEREST 2.0- and TFAW-detrended light curves. In addition, the biases and uncertainties of the fitted transit parameter values for two known K2 planetary systems (K2-44 b and K2-298 b) are also compared for both TFAW- and EVEREST 2.0-detrended light curves. In Section 4, we present the transit search and vetting criteria employed with our TFAW light curves from K2 observing campaign 1, compare our transit search results with the ones from other groups and, finally, we present two new statistically validated Earth-sized candidate planets found using TFAW-corrected light curves and TLS.

2 TFAW-DETRENDING ALGORITHM

TFAW (del Ser et al. 2018) combines the detrending and systematics removal capabilities of TFA with the signal decoupling and denoising potential of the wavelet transform. The noise contribution and the underlying signal shape are iteratively estimated from the target light curve using the Stationary Wavelet Transform (SWT). This allows TFAW to denoise and reconstruct the signal without modifying any of its astrophysical properties, i.e. without introducing artificial distortions in the signal's shape or ripples around discontinuities.

The TFAW-detrending algorithm can be summarized as follows (see del Ser et al. 2018, for further details): (1) an initial filter is computed, as with the original TFA, by means of a template of reference stars, to remove trends and systematics from the target light curve; (2) the signal shape of the detrended light curve is inferred by means of the SWT decomposition levels and its corresponding power spectrum. The outliers from the light curve are removed and a first estimation of the high-frequency noise contribution is removed using the lowest SWT decomposition level (i.e. the one with highest frequency resolution); (3) frequency analysis step: a search for significant periodicities is run over this outlier-free and denoised signal; (4) if a significant periodicity is found, the shape of the trend- and noise-free phase-folded signal is estimated again using the SWT; and (5) signal reconstruction step: the trend-free light curve is iteratively denoised and reconstructed during TFAW signal reconstruction process.

The original TFAW implementation used the BLS algorithm (Kovács, Zucker & Mazeh 2002) to search for significant transit-like periodicities within the target light curves. We have extended the algorithm capabilities to detected transits of smaller planets by using the TLS algorithm that takes the stellar limb darkening and planetary ingress and egress into account. We consider a periodicity to be significant if it corresponds to the highest peak in the TLS power spectrum and its signal detection efficiency (SDE_{TLS}) value is above 9.0. Any light curve that matches this criterion during TFAW's signal detection step will undergo the iterative signal reconstruction and denoising.

3 TFAW VERSUS EVEREST 2.0 PERFORMANCE

In del Ser et al. (2018), we show that TFAW improves the detection rate, denoising, and characterization of different astrophysical periodic signals compared to TFA. In this section, we want to assess TFAW's performance when applied to non-median filtered (to avoid removing any stellar variability of interest) EVEREST 2.0 light curves from the K2 mission. We do so by measuring the 6 h CDPP (Christiansen et al. 2012; Luger et al. 2018) for TFA, TFAW, and EVEREST 2.0, the transit detection efficiency obtained with TFAW and EVEREST 2.0, and comparing the biases and uncertainties of the Markov chain Monte Carlo (MCMC) fitted transit parameter values for two known K2 planetary systems for TFAW denoised and reconstructed light curves and the EVEREST 2.0 originals.

Table 1. The number of EVEREST 2.0 LC light curves used by TFA and TFAW for different K2 campaigns. C9 is not considered. C10 and C11 are not used because both are split in separate subcampaigns.

K2 campaign	EVEREST 2.0 light curves
C1	18 703
C2	13 394
C3	14 151
C4	15 539
C5	23 074
C6	27 435
C7	13 483
C8	21 387
C12	27 524
C13	21 407
C14	19 230
C15	22 814
C16	23 506
C17	30 931
C18	19 053

3.1 Data selection

To run TFAW, we download all the EVEREST 2.0 light curves from the K2 mission monitoring campaigns C1–C8, and C12–C18 available at the MAST archive[2] earlier than 2019 January 4. We do not consider light curves from campaigns C9 (used to study gravitational microlensing events), and from C10 to C11 (they are both split in separate subcampaigns due to a pointing and initial roll-angle error, respectively). For this work, we focus only on the long-cadence (LC) light curves as the number of available template stars per CCD module is greater than that for the short-cadence (SC) data. Table 1 lists the number of EVEREST 2.0 light curves for each K2 campaign used in this work.

Given that the SWT needs an even number of data points to work, for campaigns C1–C8 we use 3072 epochs and 2432 for campaigns C12–C18. This way we ensure a good number SWT decomposition levels (10 and 7, respectively) to determine the signal and noise contributions of the light curves while keeping enough epochs to run the periodic signal search. As neither TFA or TFAW are designed to deal with PLD (Deming et al. 2015), we use the PLD, single co-trending basis vector (CBV)-corrected fluxes provided by the EVEREST 2.0 pipeline. For all light curves, only epochs with the QUALITY = 0 flag are considered (as described in Luger et al. 2018) and extreme outliers are removed prior to the analysis.

3.2 CDPP

As a figure of merit to compare EVEREST 2.0, TFA, and TFAW photometric performance, we adopt the 6 h CDPP. In practice, we use the same CDPP metric as EVEREST 2.0, the one computed by smoothing the light curve with a 2-d, quadratic Savitsky–Golay filter,

[2]https://archive.stsci.edu/hlsps/everest/v2/bundles/

Downloaded from https://academic.oup.com/mnras/article/498/2/2778/5894404 by guest on 10 November 2023

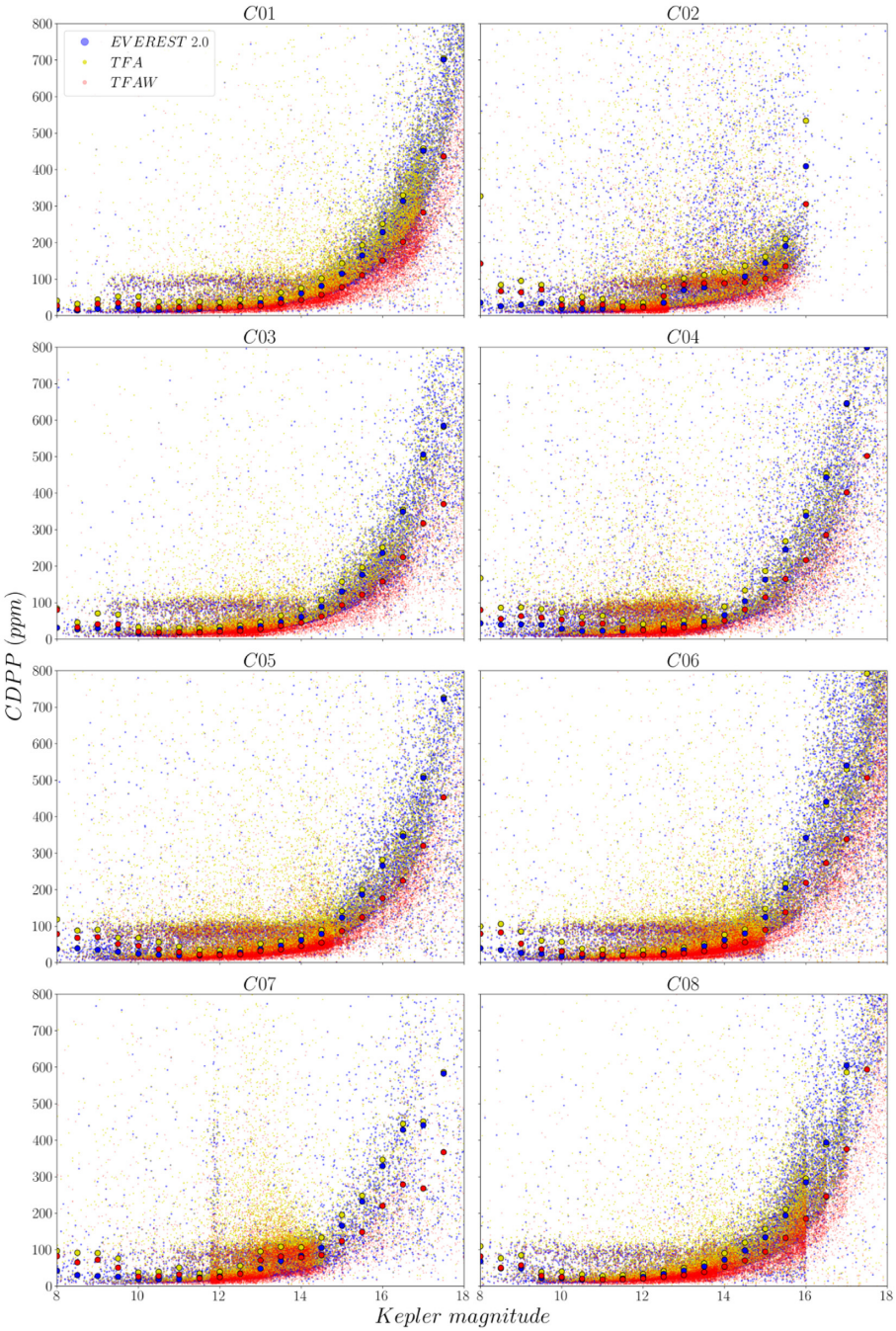

Figure 1. 6 h CDPP as a function of K_p for all K2 targets in campaigns C1–C8 corrected with `EVEREST 2.0` (blue), `TFA` (yellow), and `TFAW` (red). The median in 0.5 mag-wide bins is indicated by blue circles for `EVEREST 2.0`, by yellow circles for `TFA`, and by red circles for `TFAW`.

clipping outliers at 5σ, computing the median standard deviation in 13 cadence segments, and normalizing by $\sqrt{13}$. Though it might not be appropriate for very large amplitude or very short period variabilities, we choose the 6 h time-scale on purpose as it is roughly the transit duration of an Earth–Sun analogue (Christiansen et al. 2012).

The 6 h CDPP values computed for all `EVEREST 2.0` (blue dots), `TFA` (yellow dots), and `TFAW` (red dots) K2-detrended light curves are shown in Figs 1 (campaigns C1–C8) and 2 (campaigns C12–C18).

In accordance with the results obtained in del Ser et al. (2018), the 6 h CDPPs of `TFA` light curves clearly underperform compared to the `TFAW` ones. They are also worse when compared to the CDPPs obtained with `EVEREST 2.0` for most K_p magnitudes and most campaigns. In the best scenarios, `TFA` is only able to give similar CDPPs to the ones obtained by `EVEREST 2.0`. Given that `TFAW` outperforms `TFA` in all campaigns and magnitude ranges, we focus on the former for other performance comparisons in this paper.

Figs 3 (campaigns C1–C8) and 4 (campaigns C12–C18) show the relative 6 h CDPP differences between the `TFAW`-corrected light curves and those produced by `EVEREST 2.0` as a function of K_p magnitude. Individual CDPP values for each star are plotted as blue points and the median in 0.5 mag-wide bins as a black solid line.

Downloaded from https://academic.oup.com/mnras/article/498/2/2778/5894404 by guest on 10 November 2023

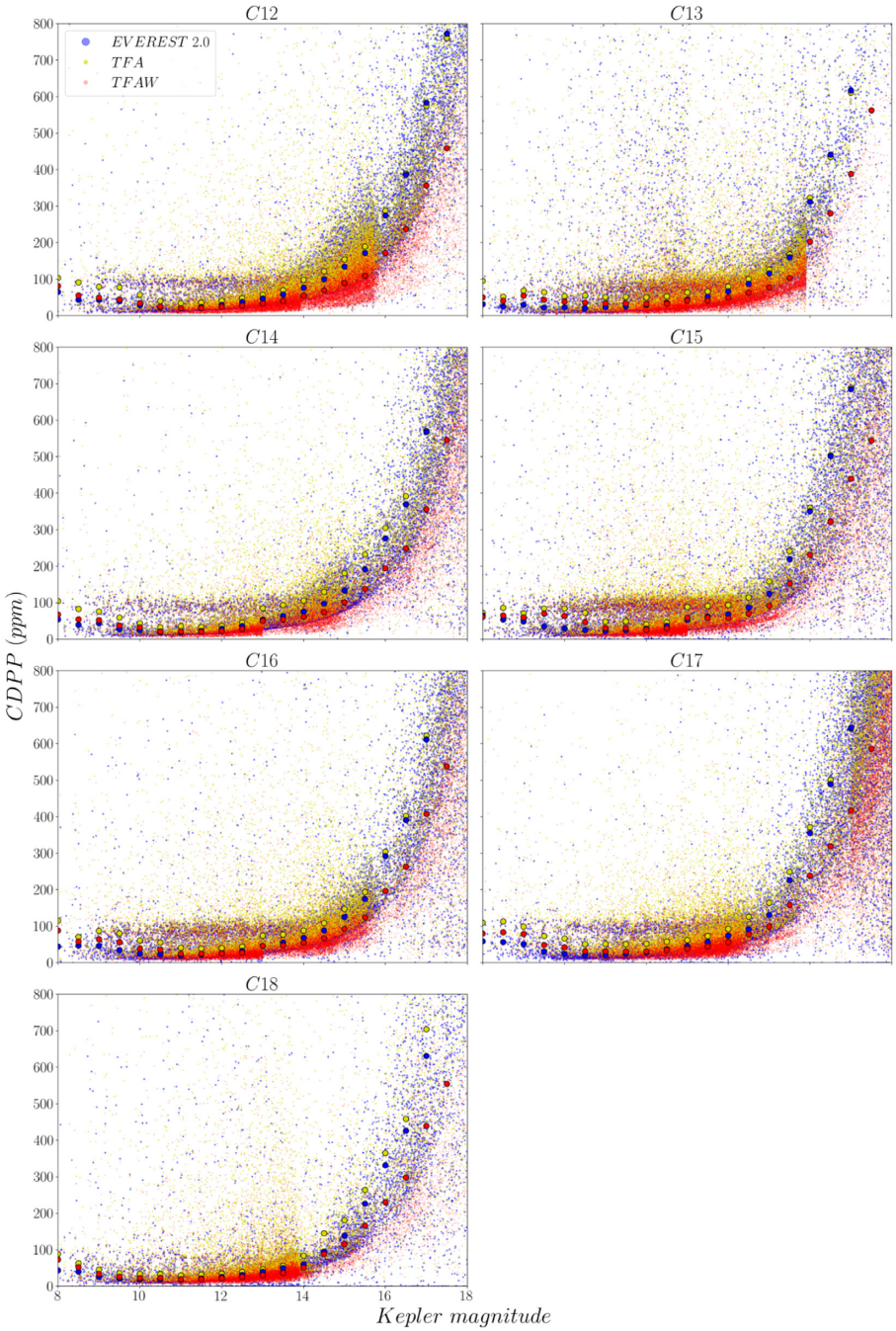

Figure 2. 6 h CDPP as a function of K_p for all K2 targets in campaigns C12–C18 corrected with `EVEREST 2.0` (blue), `TFA` (yellow), and `TFAW` (red). The median in 0.5 mag-wide bins is indicated by blue circles for `EVEREST 2.0`, by yellow circles for `TFA`, and by red circles for `TFAW`.

Saturated stars ($K_p \lesssim 11$; Luger et al. 2018) are plotted as red points, with their median indicated by a red solid line. Light curves that have undergone `TFAW` iterative reconstruction step (i.e. those with a periodicity with SDE ≥ 9.0) and those that have only had removed a first SWT estimation of the high-frequency noise have been included in the plots.

On average, the `TFAW` median relative 6 h CDPP is ∼30 per cent better than the one from `EVEREST 2.0` for stars within $11 < K_p < 15$. For saturated stars (i.e. $K_p < 11$), plotted as red dots, `TFAW` yields similar results as `EVEREST 2.0`, though many of the stars benefit from a slight improvement of about ∼5–10 per cent better CDPP values. For bright stars with $11 < K_p \lesssim 12.5$, `TFAW` light curves have higher precision than those of `EVEREST 2.0` by ∼5–25 per cent. This improvement increases as we go towards fainter magnitudes and can reach about ∼35–40 per cent better precision. This average `TFAW` performance is slightly worse for two campaigns: C2 for the larger fraction of (variable) giant stars, and C7 due to a change in the orientation of the spacecraft and excess of jitter. Overall, `TFAW` improves the photometric precision of `EVEREST 2.0` light curves for all campaigns and all K_p magnitudes, showing the robustness of `TFAW` to denoise light curves with different noise properties and coming from different stellar populations.

Downloaded from https://academic.oup.com/mnras/article/498/2/2778/5894404 by guest on 10 November 2023

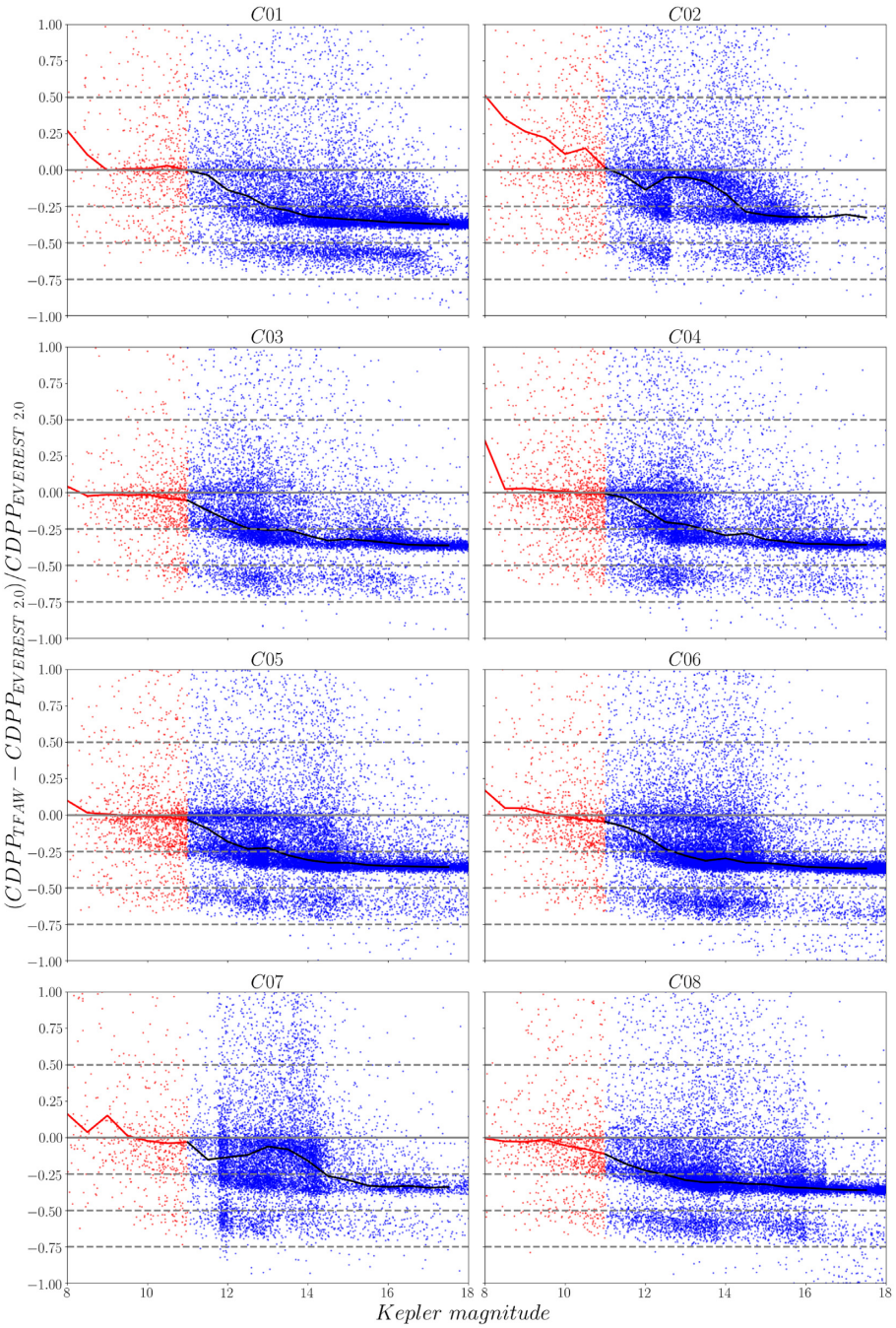

Figure 3. TFAW versus EVEREST 2.0 relative 6 h CDPP comparison for all K2 stars in campaigns C1–C8. Individual stars are plotted as points, red for saturated stars ($K_p \lesssim 11$ mag), and blue for fainter. Median relative 6 h CDPP is plotted by a solid red line, for saturated stars ($K_p \lesssim 11$ mag), and a solid black line for fainter magnitudes.

We also note in Figs 3 and 4 that the relative 6 h CDPP appears to be decoupled in three horizontal bands: one following the median, another close to zero relative CDPP, and the last one below the median with less points but evenly distributed for all K_p magnitudes. All light curves pertaining to this lower CDPP population have $SDE_{TLS} \geq 9.0$ and thus, they have undergone the iterative signal reconstruction and denoising. For these objects, TFAW has removed most of the high-frequency noise contribution leading to an ∼50–75 per cent improvement in their CDPPs. The population following the median is comprised by those light curves with $SDE_{TLS} < 9.0$, which have only a first SWT estimation of the noise removed from them during TFAW's signal detection step (see Section 2). Finally, the population close to zero relative CDPP corresponds to the horizontal branch also observed in the CDPP versus K_p plots in Figs 1 and 2. This clump of stars is giants (Christiansen et al. 2012) with short-time-scale pulsations that have not been filtered by TFAW's SWT high-frequency noise estimation. These pulsations are not efficiently captured by the high-pass filter applied during the CDPP computation (Luger et al. 2016) leading to higher values. It has to be mentioned that we have run TFAW denoising using only the lowest SWT decomposition

Downloaded from https://academic.oup.com/mnras/article/498/2/2778/5894404 by guest on 10 November 2023

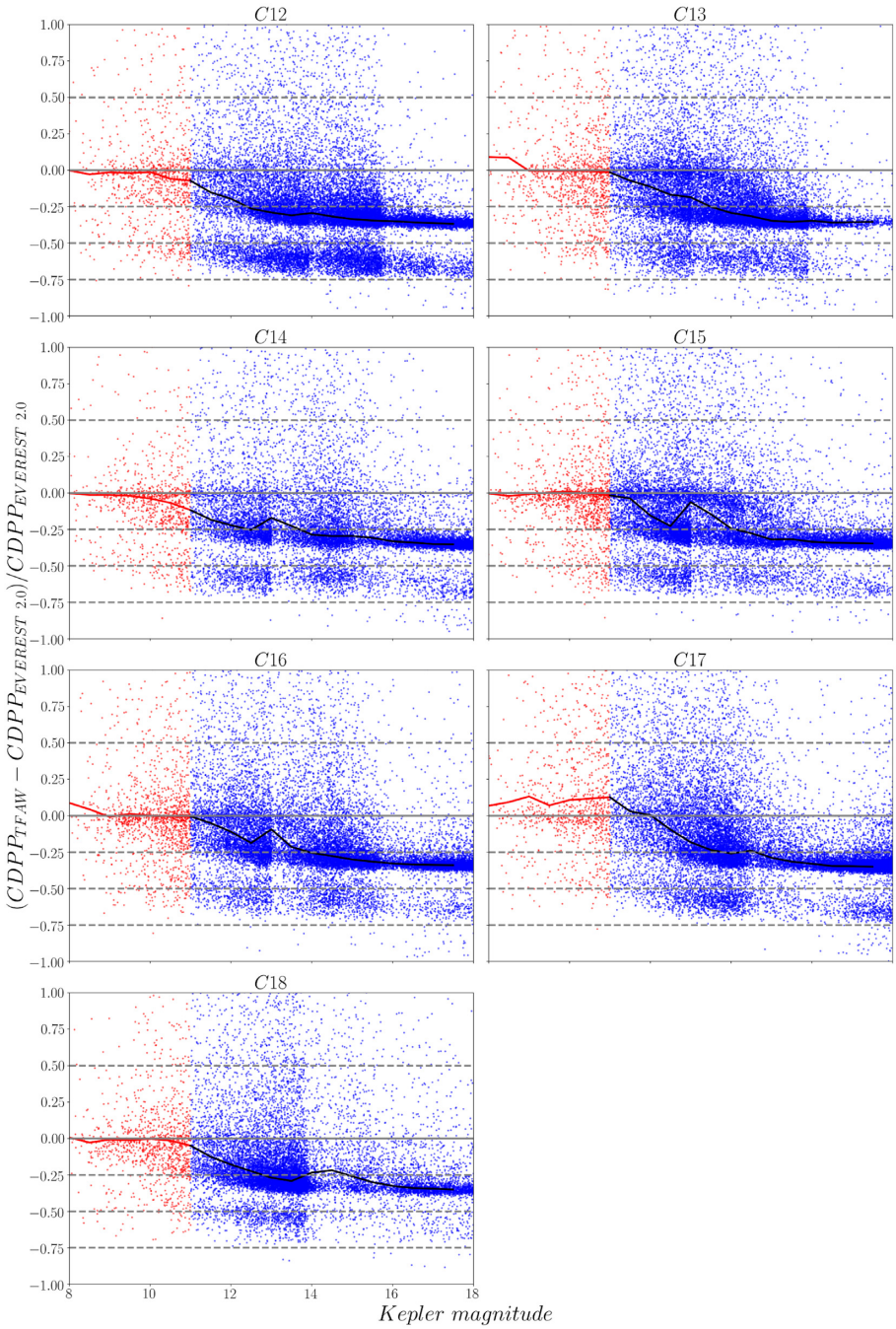

Figure 4. TFAW versus EVEREST 2.0 relative 6 h CDPP comparison for all K2 stars in campaigns C12–C18. Individual stars are plotted as points, red for saturated stars ($K_p \lesssim 11$ mag), and blue for fainter. Median relative 6 h CDPP is plotted by a solid red line, for saturated stars ($K_p \lesssim 11$ mag), and a solid black line for fainter magnitudes.

level (see Section 2) to minimize the possibility of removing high-frequency signals of stellar origin that could be of interest. However, the use of more SWT levels could benefit the CDPPs of this giant population (and of all the other stars in general) as they would remove noise/signals within a broader frequency range.

3.3 Transit detection efficiency

To assess the transit recovery rate, we generate two sets of 5000 randomly distributed test light curves covering magnitudes from $K_p = 8$ to 18, one simulating EVEREST 2.0 light curves and the other simulating light curves during TFAW's frequency analysis step. The noise contribution for each of these light curves is estimated by fitting the EVEREST 2.0 and TFAW 6 h CDDPs from Figs 1 and 2. After random white noise is injected, for each light curve at a given K_p value, its corresponding CDPP value is randomly distributed, within a given width, around the fitted value.

To each of these light curves, we inject a transit signal selected from a random distribution of Sun-like (0.7–1.35 $R_\odot$ and 0.8–1.5 $M_\odot$) and Earth-like (0.5–2.3$R_\oplus$) systems with a random distribution of periods and transit epochs (ensuring at least two

Downloaded from https://academic.oup.com/mnras/article/498/2/2778/5894404 by guest on 10 November 2023

Table 2. Mutually exclusive detections and mean SDE values for 5000 simulated transits in Earth–Sun-like systems. $N_{\rm EVEREST}$: not detected using TFAW light curves, but detected using the EVEREST 2.0 data. $N_{\rm TFAW}$: detected using TFAW light curves, but not detected using the EVEREST 2.0 data. $N_{\rm mut}$: simultaneous detections with EVEREST 2.0 and TFAW. $\rm SDE_{EVEREST}$: mean EVEREST 2.0 $\rm SDE_{TLS}$. $\rm SDE_{TFAW}$: mean TFAW $\rm SDE_{TLS}$. Percentage values in parenthesis are with respect to the 5000 tested transits.

$N_{\rm EVEREST}$	$N_{\rm TFAW}$	$N_{\rm mut}$	$\rm SDE_{EVEREST}$	$\rm SDE_{TFAW}$
80 (1.6 per cent)	681 (13.6 per cent)	2652 (53.1 per cent)	22.48 –	24.71 –

detectable transits), solar-like quadratic limb darkening coefficients, orbit inclinations, and eccentricities.

We want to compare the transit detection rates obtained with EVEREST 2.0 and TFAW light curves using TLS. We use the following criteria to define a significant detection: first, the highest peak in the TLS power spectrum must have a period between $[P_s - 0.01, P_s + 0.01]$, where P_s is the period of the simulated planetary transit, and secondly, the $\rm SDE_{TLS}$ of the highest peak in the power spectrum must be greater than 9.

We run TLS using the stellar limb darkening coefficients associated with each of the light curves and the transit search is done in the (0.01, 31.5) d range. We count the number of times the signal is detected in the TFAW light curves but not detected in the EVEREST 2.0 ones and the opposite test. Table 2 shows the number of non-simultaneous detections (both in absolute and percentage) for the 5000 simulated Earth–Sun-like systems along the K_p range for both EVEREST 2.0 and TFAW light curves. The number of non-simultaneous detections for the case of TFAW is a factor ∼8.5× higher than that for the case of EVEREST 2.0 light curves. Also, the mean $\rm SDE_{TLS}$ values are higher for TFAW than those for EVEREST 2.0. We also checked the false probability detection rate by seeing how many times the highest, non-aliased to the injected period peak in the power spectra crossed the threshold. We find similar results for EVEREST 2.0 and TFAW: 72 and 80 false detections, respectively.

Table 3 shows the distribution of the EVEREST 2.0 and TFAW detections in three K_p magnitude bins. In the bright-end regime TFAW shows 2.8× the number of detections of EVEREST 2.0. In the mid-K_p range ($11.0 < K_p < 15.0$), TFAW performs 8.9× better than EVEREST 2.0. Finally, in the faint-end case ($K_p > 15.0$), TFAW detects the transit in 21.1× more light curves than EVEREST 2.0. This increase in the detection rate is in accordance with the improvement in the CDPP values for mid- and faint-magnitude range obtained with TFAW (see Figs 3 and 4).

3.4 Transit injections

In del Ser et al. (2018) we show that, thanks to the wavelet approximation of the signal, TFAW is able to diminish the bias in the transit parameters. In order to ensure that TFAW returns an unbiased set of transit parameters, we run a transit injection/recovery test similar to the one used by Luger et al. (2016). We use a set of 2-d Savitsky–Golay filtered EVEREST 2.0 real K2 light curves with no known transit. We randomly select a sample of 3400 stars from campaigns C1–C8 and C12–C18 with $8 \leq K_p \leq 18$ mag. Using the batman[3] package (Kreidberg 2015), the catalogued stellar properties (i.e. stellar mass and radius and quadratic limb darkening coefficients) for each target, assuming circular orbits, and randomly selecting the transit parameters (planetary radius-to-stellar radius ratio, orbital period, orbit inclination, and transit epoch), we inject one planet (from a hot Jupiter to an Earth-sized planet) transit into each selected EVEREST 2.0 light curve. The injected transit depths range from $\sim 5 \cdot 10^{-5}$ to $\sim 10^{-2}$. We then run TFAW to reconstruct and denoise the light curves. To determine whether the TFAW-corrected light curves can bias the transit depths, we fix all the parameters except for the planetary radius-to-stellar radius ratio, p, at their true values and recover the latter. We fit the transit depth of the TFAW-corrected light curves by minimizing the residuals using the Levenberg–Marquardt method implemented in the lmfit package.[4] Fig. 5 shows the histogram of the recovered planetary radius-to-stellar radius ratio as a fraction of the injected one (p/p_0). As can be seen, the median p/p_0 for TFAW-reconstructed transits is consistent with 1.0. We find a small <∼2.5 per cent bias towards smaller ratios for some of the transits. This bias starts to be significant for $p < \sim 0.011$ (i.e. transit depth smaller than $\sim 10^{-4}$). However, the relative difference between p_0 and the recovered planetary radius-to-stellar radius ratio is smaller than ∼0.0005 for almost all (∼97 per cent) the simulated transits.

3.5 Characterization of known planets

In del Ser et al. (2018), we show that TFAW can improve the MCMC posterior distributions, diminish the bias in the fitted transit parameters and their uncertainties, and narrow the credibility intervals for simulated transits. In this section, we compare EVEREST 2.0 and TFAW performances in terms of assessing the bias of the MCMC fitted transit parameter values and their uncertainties for two confirmed planetary systems with different SNRs: K2-44 b and K2-298 b.

3.5.1 Data description

As the starting point for the computation of TFAW, we use the PLD, CBV-corrected fluxes provided by the EVEREST 2.0 pipeline for both targets and all stars present in the same campaign and CCD module. 3072 epochs with the QUALITY = 0 flag are considered and a 2-d Savitsky–Golay filter and a 5σ outlier clipping are applied to the light curves. To iteratively denoise and reconstruct the light curves with TFAW, a template of reference stars for each target (∼90) is built from a subset of stars from the same CCD module using Stetson's L variability index (Stetson 1996) to avoid the inclusion of bona fide variable stars in the sample. We use this TFAW-corrected light curve to run the MCMC fit and compare it to the one obtained from the EVEREST 2.0 light curve.

Prior to the TFAW analysis, for both K2-44 b and K2-298 b we checked that the light curves we obtained directly from the EVEREST 2.0 matched with the ones after the transits have been masked. This way, we ensure that any bias in the depth of the transiting planet is minimized (Luger et al. 2018).

3.5.2 Transit parameters fitting procedure

To characterize the target transits, we use the analytic transiting model provided by the batman package with quadratic limb darkening coefficients as per Mandel & Agol (2002). We assume circular orbits (i.e. eccentricity = 0) and fit the following five transit parameters: the transit epoch, T_0, the orbital period, P, the semimajor

[3] https://www.cfa.harvard.edu/~lkreidberg/batman/

[4] https://doi.org/10.5281/zenodo.3814709

Downloaded from https://academic.oup.com/mnras/article/498/2/2778/5894404 by guest on 10 November 2023

Table 3. Detection distributions of ($N_{\rm EVEREST}$, $N_{\rm TFAW}$, and $N_{\rm mut}$) for the 5000 simulated Earth–Sun-like systems as per three bins of $K_{\rm p}$ magnitude.

$K_{\rm p} < 11.0$			$11.0 < K_{\rm p} < 15.0$			$K_{\rm p} > 15.0$		
$N_{\rm EVEREST2.0}$	$N_{\rm TFAW}$	$N_{\rm mut}$	$N_{\rm EVEREST2.0}$	$N_{\rm TFAW}$	$N_{\rm mut}$	$N_{\rm EVEREST2.0}$	$N_{\rm TFAW}$	$N_{\rm mut}$
32	90	1290	36	338	1283	12	253	79

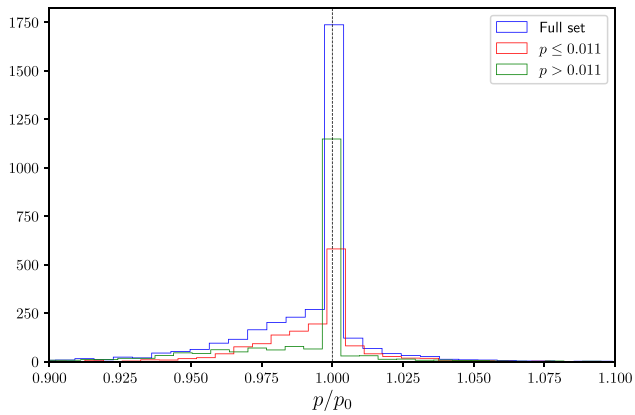

Figure 5. Histogram of transits with a certain planetary radius-to-stellar radius ratio as a fraction of the injected one (p/p_0) recovered after TFAW's signal reconstruction step. The blue histogram corresponds to the 3400 recovered transits, the red histogram corresponds to those injected transits with $p \leq 0.011$, and the green histogram corresponds to transits with $p > 0.011$.

axis of the orbit, a, the planetary radius-to-stellar radius ratio, p, and the inclination of the orbit, i. We use the MCMC sampler provided by the emcee (Foreman-Mackey et al. 2013) package and use the george (Ambikasaran et al. 2015) package to create a combined model consisting on a Matérn 3/2 kernel plus a jitter or 'white' noise term to generalize the likelihood function in order to consider covariances between data points (i.e. correlated noise) and to minimize the bias of the inferred parameters. We consider a uniform distribution of the priors with wide enough bounds to let the chains explore the parameter space without getting close to the bound limit: ±1 d around the catalogued transit epoch for T_0, ±3 d for P, from $2R_*$ to the catalogued semimajor axis plus $5R_*$ for a, the catalogued planet/star ratio ±0.01 for p, and from 85° to 90° for i. We run the sampler with 100 walkers, 10 000 iterations with a burn-in phase of 2000 iterations. This way, we ensure that each of the chains runs for more than 50 autocorrelation times for each parameter and that the mean acceptance fraction is between 0.25 and 0.5 (Bernardo et al. 1996; Foreman-Mackey et al. 2013).

3.5.3 K2-44: a confirmed high-SNR single planetary system example

K2-44 (EPIC 201295312) is a $V = 12.19 \pm 0.12$ mag (Zacharias et al. 2012) located at (α, δ) = (11:36:02.79, −02:31:15.17) (Gaia Collaboration 2018). It was observed by the K2 mission during the C1 monitoring campaign from 2014 May 30 to Aug 21. K2-44 was first reported as a planetary hosting candidate by Montet et al. (2015), and later validated, confirmed, and characterized by Crossfield et al. (2016) and Mayo et al. (2018). For a more detailed summary of the stellar and planetary parameters, see Table 4.

To check whether the improved photometric precision yielded by TFAW in Section 3.2 results in a better characterization of the transiting signal, we analyse EVEREST 2.0- and TFAW-corrected light curves for the confirmed exoplanet K2-44 b and compare the fitted parameters with the ones obtained by Crossfield et al. (2016) and Mayo et al. (2018). We assume a circular orbit ($e = 0$) and a longitude of the periastron of $\omega = 90°$. Using the stellar parameters provided by Crossfield et al. (2016) (see Table 4) and assuming a metallicity of [Fe/H] = 0.0, we fix the quadratic limb darkening coefficients to their theoretical values taken from Claret (2018).

Table 4. Stellar and planetary parameters obtained for K2-44 b by Crossfield et al. (2016), Sing (2010), and Mayo et al. (2018).

K2 ID	EPIC 201295312
Stellar parameters	
Stellar radius $R_{\rm s}$ ($R_\odot$)	1.58 ± 0.15
Stellar mass $M_{\rm s}$ ($M_\odot$)	1.150 ± 0.060
Effective temperature (K)	5912 ± 51
Surface gravity [$\log_{10}$(cm s^{-2})]	4.101 ± 0.063
Metallicity [Fe/H]	0.0 (assumed)
Spectral type	–
Transit parameters	
Period P (days)	5.656 88 ± 0.000 59
Transit epoch T_0 (BJD – 2454833) (days)	1978.7176 ± 0.0044
Transit duration (hours)	4.36 ± 0.13
Eccentricity e	0 (assumed)
Radius ratio p	0.0156 ± 0.0012
q_1	0.4752[a]
q_2	0.1914[a]
Scaled semimajor axis a (au)	0.0651 ± 0.0011
Inclination i (°)	$87.354\,350^{+1.856\,108}_{-3.300\,347}$[b]
Planetary parameters	
Planetary radius $R_{\rm p}$ ($R_\oplus$)	2.72 ± 0.32

Notes. [a]Denotes values from Claret (2018) assuming 0.0 [Fe/H] metallicity. [b]Denotes values from Mayo et al. (2018).

In Table 5, we compare the transit parameters and their uncertainties obtained by Crossfield et al. (2016) and Mayo et al. (2018) with the ones obtained with EVEREST 2.0 and TFAW posterior probability distributions after running the MCMC fit as indicated in Section 3.5.2. The fitted parameter values are obtained from the 50 per cent quantiles and their upper and lower errors are computed from the 25 and 75 per cent quantiles, respectively.

The MCMC fit corner plot (Foreman-Mackey 2016) for the K2-44 b transit is shown in Fig. 6, yielding the following results: the time of inferior conjunction, T_0, for EVEREST 2.0 and TFAW is compatible with the one reported by Crossfield et al. (2016) and Mayo et al. (2018), though for TFAW, the uncertainties are much lower than those for the other three [∼2× for EVEREST 2.0, ∼2.5× for Mayo et al. (2018), and ∼4× compared to Crossfield et al. (2016)]. For the semimajor axis of the orbit, a, EVEREST 2.0 and TFAW return smaller values than the one by Crossfield et al. (2016). However, while EVEREST 2.0 value is compatible within the errors with the one reported by Crossfield et al. (2016), this is not the case of TFAW. However, it is still compatible if one takes into account the uncertainties in the stellar radius, impact parameter, and orbit inclination. For the latter, both EVEREST

Downloaded from https://academic.oup.com/mnras/article/498/2/2778/5894404 by guest on 10 November 2023

Table 5. Top table: K2-44 b parameters from Crossfield et al. (2016), Mayo et al. (2018), and posterior transit parameter values and their uncertainties (25 and 75 per cent quantiles) for EVEREST 2.0 and TFAW MCMC fits. Middle table: 95 per cent confidence intervals of the highest probability density for K2-44 b transit parameters EVEREST 2.0 and TFAW MCMC fits. Bottom table: Derived parameters from Crossfield et al. (2016), Mayo et al. (2018), EVEREST 2.0, and TFAW.

MCMC parameters	T_0 (BJD-2454833)	P (d)	a (au)	p	i (°)
Crossfield et al. (2016)	1978.7176 ± 0.0044	$5.656\,88 \pm 0.000\,59$	0.0651 ± 0.0011	0.0156 ± 0.0012	–
Mayo et al. (2018)	$1978.72011^{+0.002\,565}_{-0.002\,557}$	$5.656\,304^{+0.000\,366}_{-0.000\,323}$	–	$0.017\,257^{+0.000\,704}_{-0.000\,538}$	$87.354\,350^{+1.856\,108}_{-3.300\,347}$
EVEREST 2.0	$1978.7248^{+0.0020}_{-0.0019}$	5.6549 ± 0.0003	$0.0644^{+0.0030}_{-0.0048}$	0.0149 ± 0.0005	$87.7663^{+1.1671}_{-1.3999}$
TFAW	$1978.7094^{+0.0012}_{-0.0011}$	5.6570 ± 0.0002	$0.0600^{+0.0019}_{-0.0029}$	$0.0141^{+0.0005}_{-0.0004}$	$87.9933^{+1.0218}_{-1.1633}$
95 per cent confidence intervals of the highest posterior density					
EVEREST 2.0	1978.71873–1978.73143	5.653 91–5.655 98	0.053 10–0.070 49	0.013 42–0.016 45	84.960 43–89.999 88
TFAW	1978.70600–1978.71302	5.656 38–5.657 57	0.053 08–0.063 93	0.013 02–0.015 56	85.668 26–89.999 71

Derived system parameters	R_p ($R_\oplus$)	b
Crossfield et al. (2016)	2.72 ± 0.32	–
Mayo et al. (2018)	$2.939\,205\,842\,11^{+0.496\,465\,103\,254}_{-0.376\,603\,037\,856}$	–
EVEREST 2.0	$2.571^{+0.089}_{-0.089}$	$0.34^{+0.18}_{-0.21}$
TFAW	$2.433^{+0.089}_{-0.072}$	$0.29^{+0.15}_{-0.17}$

2.0 and TFAW yield values compatible with the reported value by Mayo et al. (2018). Again, TFAW returns the smallest uncertainties. Regarding the planetary-to-star radius ratio, p, both EVEREST 2.0 and TFAW obtain compatible values within the errors with the one reported by Crossfield et al. (2016). Again, TFAW returns the smallest uncertainties for this parameter and compatible with the p/p_0 dispersion seen in Fig. 5. For the period, P, the values from TFAW and EVEREST 2.0 are compatible with the catalogued ones. As for the previous parameters, TFAW returns the smallest uncertainties for the period. In summary, even for this rather high-SNR transit, TFAW returns lower uncertainties for all parameters compared with the EVEREST 2.0 and catalogued ones. Also, following the results in del Ser et al. (2018) with simulated transits, the transit parameters obtained with TFAW might be closer to the real ones (assuming that the planet orbits in a circular orbit). Finally, the widths of TFAW's 95 per cent confidence intervals are narrower for all parameters.

With the best-fitting parameters, EVEREST 2.0 obtains a mean planetary radius of 2.571 ± 0.089 $R_\oplus$ and TFAW $2.433^{+0.089}_{-0.072}$ $R_\oplus$, both slightly below the values reported by Crossfield et al. (2016) and Mayo et al. (2018), but compatible within the errors. Although b is not reported either by Crossfield et al. (2016) or Mayo et al. (2018), we also derive it from the best-fitting parameters for EVEREST 2.0 to be $0.34^{+0.18}_{-0.21}$, and for TFAW to be $0.29^{+0.15}_{-0.17}$.

Fig. 7 shows the summary plot displaying the PLD, CBV-corrected flux provided by the EVEREST 2.0 pipeline for K2-44 with the 2-d running median plotted in red, the EVEREST 2.0 median-filtered light curve and the TFAW-corrected light curves (with the MCMC-derived transit data of the new candidate plotted in red), the TLS periodograms for EVEREST 2.0 and TFAW's frequency analysis step, and the phase-folded light curves with the MCMC fit data (red line) for EVEREST 2.0 (left) and TFAW iteratively denoised and reconstructed one (right). The TLS periodograms show the position of the confirmed planet detected period (solid blue line) and its harmonics (dashed blue lines).

3.5.4 K2-298: a confirmed+candidate low-SNR multiplanetary system example

K2-298 (EPIC201841433) is a $V = 14.87 \pm 0.01$ mag (Zacharias et al. 2012) star located at $(\alpha, \delta) = (11{:}40{:}49.62, +06{:}08{:}05.44)$ (Gaia Collaboration 2018). It was observed by the K2 mission during the C1 monitoring campaign from 2014 May 30 to Aug 21. K2-298 was validated as a $0.802^{+0.081}_{-0.163}$ $M_\odot$ (Heller, Hippke & Rodenbeck 2019), $T_{\rm eff} = 5053^{+103}_{-166}$ K, $0.628\,461\,06^{+0.043\,419\,84}_{-0.024\,858\,35}$ $R_\odot$ (Gaia Collaboration 2018) star orbited by an inner planet, K2-298 b, of $1.10^{+0.14}_{-0.12}$ $R_\oplus$ at $11.5^{+5.2}_{-2.6}$ R_s (Kruse et al. 2019) with a period of $4.168\,88^{+0.000\,50}_{-0.000\,56}$ d (Heller et al. 2019), and an outer candidate, EPIC201841433.01, of $2.11^{+0.23}_{-0.61}$ $R_\oplus$ at $29.5^{+14.7}_{-6.7}$ R_s with a period of $12.3389^{+0.0016}_{-0.0017}$ d (Kruse et al. 2019). Table 6 summarizes all the stellar and planetary parameters for K2-298 b.

As with the K2-44 case, we want to check whether the improved photometric precision yielded by TFAW results in a better characterization of the transiting signal. We analyse EVEREST 2.0- and TFAW-corrected light curves for the confirmed exoplanet K2-298 b and compare the fitted parameters with the ones obtained by Heller et al. (2019) and Kruse et al. (2019). We, again, assume a circular orbit ($e = 0.0$), and a longitude of the periastron of $\omega = 90°$. Using the stellar parameters in Table 6 and assuming a metallicity of [Fe/H] = 0.0, we fix the quadratic limb darkening coefficients to their theoretical values taken from Claret (2018).

In Table 7, we compare the transit parameters and their uncertainties obtained by Heller et al. (2019) and Kruse et al. (2019) with the ones obtained with EVEREST 2.0 and TFAW MCMC posterior probability distributions. As with K2-44 b, the fitted parameter values are obtained from the 50 per cent quantiles and their upper and lower errors are computed from the 25 and 75 per cent quantiles, respectively.

For the best fit (shown in Fig. 8), the mid-transit, T_0, for EVEREST 2.0 and TFAW is compatible with the one reported by Kruse et al. (2019), though for TFAW, the uncertainties are much lower than those for the other two [$\sim$2× for EVEREST 2.0, and $\sim$5× compared to Kruse et al. (2019)]. The value given by Heller et al. (2019) corresponds to the first transit after the centre of the respective K2 target light curve. For the orbit inclination, i, neither Heller et al. (2019) nor Kruse et al. (2019) report a value. However, both EVEREST 2.0 and TFAW yield values that are compatible within their errors and as with the previous parameters, TFAW returns the smallest uncertainties ($\sim$1.2× compared to EVEREST 2.0). For the period, P, the values found for EVEREST 2.0 and TFAW are compatible within the errors with the one in Heller et al. (2019) and are very close to the one in Kruse et al. (2019). Again, TFAW returns

Downloaded from https://academic.oup.com/mnras/article/498/2/2778/5894404 by guest on 10 November 2023

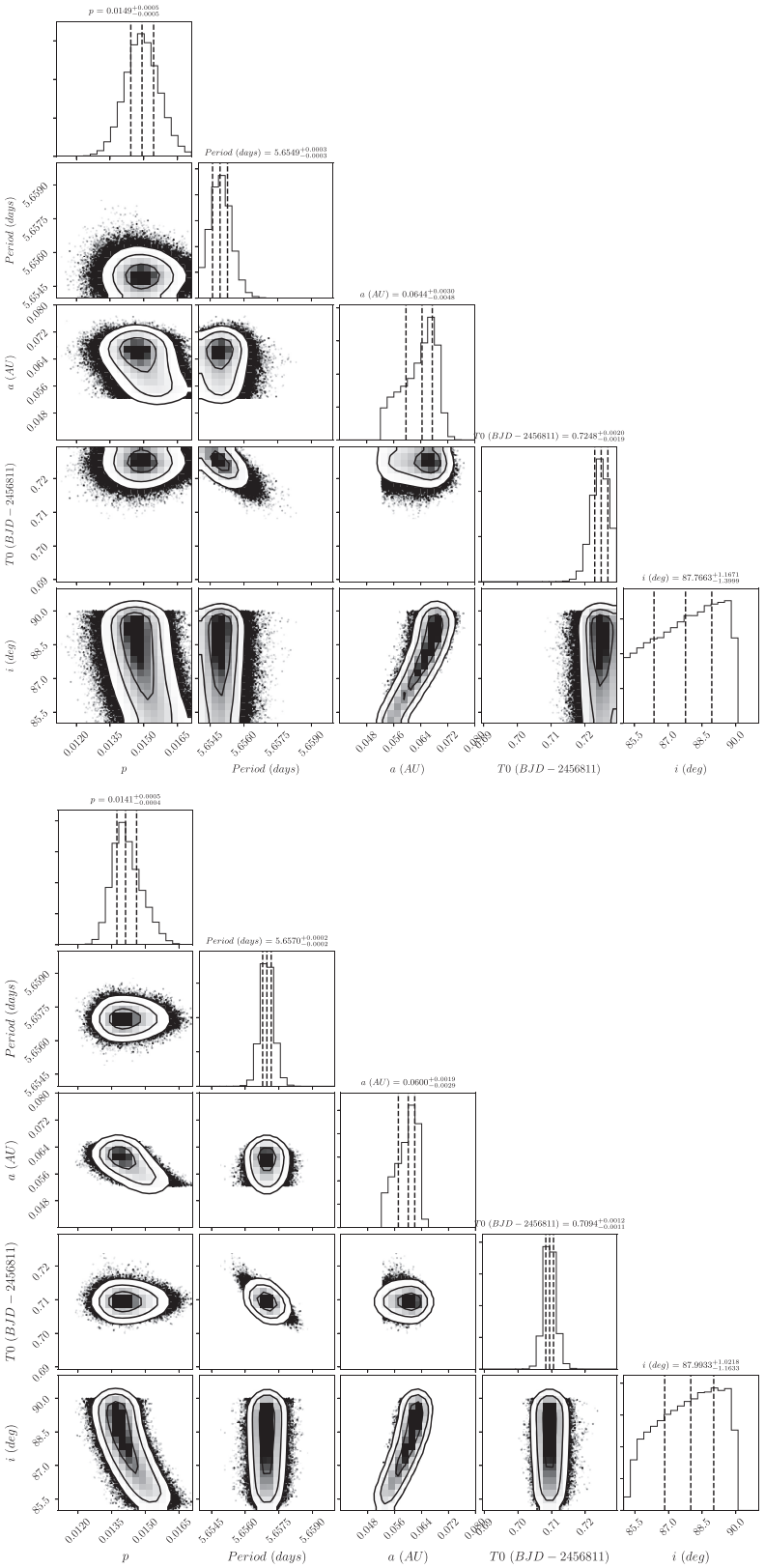

Figure 6. 1D and 2D projections of the posterior probability distributions of the five MCMC fitted parameters (p, P, a, T_0, and i) for K2-44 b `EVEREST 2.0` (top) and `TFAW` (bottom) light curves. The 25, 50, and 75 per cent quantiles are displayed in dashed vertical lines on the 1D histograms and on the top each panel column.

Downloaded from https://academic.oup.com/mnras/article/498/2/2778/5894404 by guest on 10 November 2023

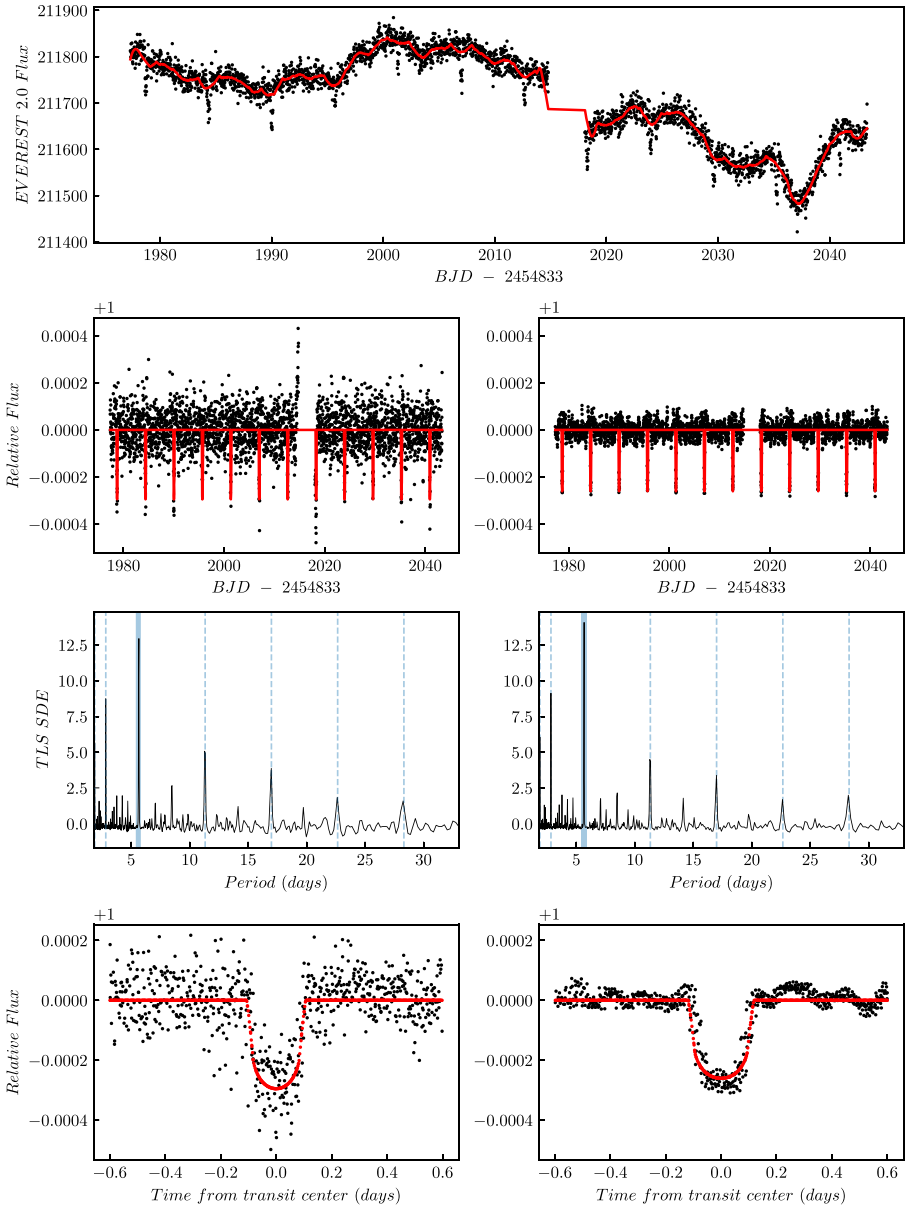

Figure 7. *From top to bottom*, the panels show the K2-44 raw flux of the EVEREST 2.0 light curve (with the running median in red), the entire light curve with in-transit data of the new candidate marked in red (left for EVEREST 2.0 and right for TFAW), the SDE_{TLS} periodogram (left for EVEREST 2.0 and right for TFAW), and the normalized phase-folded to the K2-44 b period light curve with MCMC fit data marked in red (left for EVEREST 2.0 and right for TFAW).

the smallest uncertainties for this parameter [∼3× for EVEREST 2.0, ∼5× for Heller et al. (2019) and Kruse et al. (2019)]. For the semimajor axis of the orbit, a, EVEREST 2.0 and TFAW values are compatible taking the lower errors with the one reported by Kruse et al. (2019). Again, TFAW returns the smallest uncertainties for this parameter [∼2× for EVEREST 2.0, and ∼10× compared to Kruse et al. (2019)]. Finally, regarding the planetary-to-star radius ratio, p, both EVEREST 2.0 and TFAW obtain compatible values within the errors with the one reported by Heller et al. (2019). With respect to the value reported by Kruse et al. (2019), it is compatible taking into account the reported planetary and stellar radius uncertainties. As with the other parameters, TFAW returns the smallest uncertainties for this parameter [∼2× for EVEREST 2.0, ∼7× for Kruse et al. (2019), and ∼5× compared to Heller et al. (2019)] and again, compatible with the p/p_0 dispersion seen in Fig. 5. As with K2-44 b, the widths of TFAW's 95 per cent confidence intervals are narrower for all parameters.

With the best-fitting parameters, EVEREST 2.0 obtains a mean planetary radius of $1.072^{+0.061}_{-0.054}$ $R_\oplus$ and TFAW $1.040^{+0.037}_{-0.032}$ $R_\oplus$, compatible with the $1.10^{+0.14}_{-0.12}$ $R_\oplus$ reported by Heller et al. (2019) and $1.41^{+0.15}_{-0.34}$ $R_\oplus$ reported by Kruse et al. (2019). We also derive b from the best-fitting parameters, for EVEREST 2.0 to be $0.26^{+0.14}_{-0.16}$ and for TFAW to be $0.21^{+0.11}_{-0.12}$, both compatible with the one in Heller et al. (2019). For both derived parameters, TFAW returns the lowest uncertainties.

Fig. 9 shows the summary plot displaying the PLD, CBV-corrected flux provided by the EVEREST 2.0 pipeline for K2-298 with the 2-d running median plotted in red, the EVEREST 2.0 median-filtered

Downloaded from https://academic.oup.com/mnras/article/498/2/2778/5894404 by guest on 10 November 2023

Table 6. Stellar and planetary parameters obtained for K2-298 b by Heller et al. (2019), Kruse et al. (2019), Sing (2010), Gaia Collaboration (2018), and Andrae et al. (2018).

K2 ID	EPIC 201841433
Stellar parameters	
Stellar radius R_s ($R_\odot$)	$0.628\,461\,06^{+0.043\,419\,84}_{-0.024\,858\,35}$ [d]
Stellar mass M_s ($M_\odot$)	$0.802^{+0.081}_{-0.163}$
Effective temperature (K)	5053^{+103}_{-166} [d]
Surface gravity [$\log_{10}$(cm s^{-2})]	$4.595^{+0.050}_{-2.860}$
Metallicity [Fe/H]	0.0 (assumed)
Spectral Type	–
Transit parameters	
Period P (days)	$4.169\,59^{+0.000\,51}_{-0.000\,53}$
Transit epoch T_0 (BJD – 2454833) (days)	$2020.3300^{+0.0037}_{-0.0033}$
Transit duration (hours)	$2.400^{+0.264}_{-0.336}$ [c]
Eccentricity e	0 (assumed)
Radius ratio p	$0.0160^{+0.0017}_{-0.0016}$
q_1	0.5510[a]
q_2	0.1575[a]
Scaled semimajor axis a (au)	$0.0503^{+0.0227}_{-0.0114}$ [c]
Inclination i (°)	88.21[b]
Planetary parameters	
Planetary radius R_p ($R_\oplus$)	$1.10^{+0.14}_{-0.12}$

Notes. [a]Denotes values from Claret (2018) assuming 0.0 [Fe/H] metallicity.
[b]Denotes values derived assuming $b = 0.36^{+0.24}_{-0.25}$ (Heller et al. 2019) and $a = 11.5^{+5.2}_{-2.6}$ R_s Kruse et al. (2019).
[c]Denotes values taken from Kruse et al. (2019).
[d]Denotes values derived from Gaia Collaboration (2018).

light curve and the TFAW-corrected light curves (with the MCMC-derived transit data of the new candidate plotted in red), the TLS periodograms for EVEREST 2.0 and TFAW's frequency analysis step, and the phase-folded light curves with the MCMC fit data (red line) for EVEREST 2.0 (left) and TFAW iteratively denoised and reconstructed one (right). The TLS periodograms show the position of the candidate planet detected period (Kruse et al. 2019) (solid blue line) and its harmonics (dashed blue lines) and the position of K2-298 b period (solid red line).

3.5.5 *TFAW's limitations*

The small oscillations in some of the TFAW-detrended and denoised light curves, such as in the lower right panel of Fig. 7, might be explained by one or a combination of the following three factors. First, it could be real correlated noise present in the decomposition levels above the chosen signal level that may have not been properly removed during the TFAW detrending stage. Secondly, in some cases, real stellar variability with different time-scales can be present at the same decomposition levels associated with the phased-folded transit signal. As a consequence, this stellar variability can be included in the signal estimation, reconstruction, and denoising process. Thirdly, spurious features in the signal estimation arising from the shape of the mother wavelet or an alias due to the sampling of the data in the phase-folded light curve. These two later effects cannot be fully discarded but the signal estimation can be improved by increasing the number of decomposition levels or by optimizing the signal level selection criteria. On the other hand, signals caused by stellar activity or pulsation are unique to each star and temporally correlated, and cannot be easily removed by decorrelation or denoising techniques. For example, the *bump* around phase [+0.2, +0.3] seen in the K2-44 b TFAW phase-folded light curve at the lower right panel of Fig. 7 is also present in the EVEREST 2.0 at the same phase interval. The removal of temporally correlated noise can be difficult to do using the SWT. Although this is beyond the scope of this paper, future versions of the TFAW can benefit from: the incorporation of GP to model the covariance structure of the correlated noise (Chakrabarty & Sengupta 2019), modelling of the signal of interest in the wavelet domain (Goossens, Pizurica & Philips 2009), or thresholding the wavelet coefficients (Jansen & Bultheel 1999) prior to the Inverse Stationary Wavelet Transform at each level to reduce the correlated noise. Another way to diminish the effects of correlated noise (which has a higher frequency in the phase-folded light curve than the transit signal) would be to increase the noise level or to increase the number of decomposition levels (i.e. adding more epochs to the light curve) as to better separate the different signal contributions at different frequencies. The latter is not possible with the K2 data as the number of available epochs in the archive is fixed. It is worth mentioning that we have been extremely careful when selecting the noise and signal levels to minimize the chances of removing part of the signal of interest contribution, so the results could improve by a more aggressive selection of those levels.

4 TESTING TRANSIT SEARCH WITH TFAW: TWO TRANSIT CANDIDATES IN K2 OBSERVING CAMPAIGN C1

In this section, we present partial results obtained after the application of TFAW to EVEREST 2.0 light curves from the K2 observing campaign C1. We present two new Earth-sized transiting planet candidates detected using TLS during TFAW's frequency analysis step (i.e. light curve is detrended and has had a first SWT noise estimation removed). For both cases, we show their transit parameters obtained with MCMC after TFAW's iterative signal denoising and reconstruction. A more extensive planet search, not only for C1 but also for all K2 campaigns, and using fully automatic vetting (Kostov et al. 2019; Zink et al. 2020), is underway. With this study, which is to be completed soon for an upcoming publication, we will obtain more potential new candidates.

In this section, we also compare our ability to recover confirmed and candidate transit planets detected by other searches for C1.

4.1 Data description

We use the PLD, CBV-corrected fluxes provided by the EVEREST 2.0 pipeline for K2 observing campaign C1. For each light curve, 3072 epochs with the QUALITY = 0 flag are considered. Given that the goal is to search for transiting signals, a 2-d Savitsky–Golay filter is applied to remove or minimize the effects of stellar variability. After the filter has been applied, light curves have their outliers removed using a 5σ clipping. An extra outlier removal is done by TFAW prior to the period search using a wavelet estimation of the signal (see del Ser et al. 2018, for more details). To iteratively denoise and reconstruct the light curves with TFAW, a template of reference stars for each light curve (∼90) is built from a subset of stars from the same CCD module. To avoid the inclusion of variable stars in this template, we use Stetson's L variability index (Stetson 1996).

4.2 Transit search and vetting criteria

We follow a transit search, vetting, and false-positive probability (FPP) approach similar to the one detailed in Heller et al. (2019).

Downloaded from https://academic.oup.com/mnras/article/498/2/2778/5894404 by guest on 10 November 2023

Table 7. Top table: K2-298 b parameters from Heller et al. (2019), Kruse et al. (2019), and posterior transit parameter values and their uncertainties (25 and 75 per cent quantiles) for EVEREST 2.0 and TFAW MCMC fits. Middle table: 95 per cent confidence intervals of the highest probability density for K2-298 b transit parameters EVEREST 2.0 and TFAW MCMC fits. Bottom table: Derived parameters from Heller et al. (2019), Kruse et al. (2019), EVEREST 2.0, and TFAW.

MCMC parameters	T_0 (BJD-2454833)	P (days)	a (au)	p	i (°)
Heller et al. (2019)	$2020.3300^{+0.0037}_{-0.0033}$	$4.169\,59^{+0.000\,51}_{-0.000\,53}$	–	$0.0160^{+0.0017}_{-0.0016}$	–
Kruse et al. (2019)	$1978.6338^{+0.0062}_{-0.0056}$	$4.168\,88^{+0.000\,50}_{-0.000\,56}$	$0.0503^{+0.0227}_{-0.0114}$	$0.0205^{+0.0020}_{-0.0047}$	–
EVEREST 2.0	$1978.6357^{+0.0024}_{-0.0023}$	$4.1691^{+0.0003}_{-0.0003}$	$0.0371^{+0.0026}_{-0.0020}$	$0.0156^{+0.0007}_{-0.0007}$	$88.8116^{+0.6143}_{-0.7022}$
TFAW	$1978.6359^{+0.0011}_{-0.0012}$	$4.1698^{+0.0001}_{-0.0001}$	$0.0350^{+0.0009}_{-0.0010}$	$0.0152^{+0.0004}_{-0.0003}$	$89.0010^{+0.5117}_{-0.5574}$
95 per cent confidence intervals of the highest posterior density					
EVEREST 2.0	1978.62910–1978.64271	4.168 28–4.169 92	11.116 98–15.228 17	0.013 55–0.017 96	87.206 58–89.999 99
TFAW	1978.63245–1978.63912	4.169 46–4.170 10	11.116 86–12.731 92	0.014 24–0.016 41	87.848 71–90.000 00

Derived system parameters	R_p ($R_\oplus$)	b
Heller et al. (2019)	$1.10^{+0.14}_{-0.12}$	$0.36^{+0.25}_{-0.24}$
Kruse et al. (2019)	$1.41^{+0.15}_{-0.34}$	–
EVEREST 2.0	$1.072^{+0.061}_{-0.054}$	$0.26^{+0.14}_{-0.16}$
TFAW	$1.040^{+0.037}_{-0.032}$	$0.21^{+0.11}_{-0.12}$

First, we use TLS to search for transiting signals during TFAW's frequency analysis step. TLS is run using modelled stellar parameters, M_s, R_s, u_1, and u_2. All light curves that have a TLS power spectrum peak with an SDE_{TLS} greater than 9 (false-positive rate $<10^{-4}$; Hippke & Heller 2019) are considered as a significant detection and undergo TFAW's iterative signal reconstruction and denoising. Then, we visually inspect those TFAW-corrected light curves and only keep the ones that visually show transit-like features.

Following the same procedure as Heller et al. (2019), all transits are required to have at least 0.5 d from the beginning or end of any gaps in their light curves to avoid false positives. If a candidate had three or fewer transits, they should have an SNR>10. In addition, to reject eclipsing binaries, for all candidates the average depth of the odd and even transits should agree within $<3\sigma$ and objects should not present evidence of a secondary eclipse at the $>3\sigma$ level at half an orbital phase after the candidate transit.

For those light curves we consider of interest, we include some extra vetting steps with respect to the procedure in Heller et al. (2019) to increase the reliability of the candidates. First, we perform an extensive bibliographic search of such target. We cross-match this source with the most up-to-date (2020 March 8 for this work) K2-C1 lists of confirmed or candidate exoplanets from the NASA Exoplanet Archive[5] (Akeson et al. 2013) or in the Vizier data base. We also check if the target shows any known kind of variability or pulsation (Watson, Henden & Price 2006; Armstrong et al. 2015, 2016). The updated stellar parameters and the 2MASS and SDSS photometry of the host stars are retrieved from catalogues such as EPIC (Huber et al. 2016), Gaia-DR2 (Gaia Collaboration 2018), and Claret (2018). We also search if the candidates have been observed by the *TESS* mission (Ricker et al. 2015). Secondly, we rule out that no other light curve in the same CCD module presents transit-like features with similar periods and transit epochs as the candidate. Thirdly, we compare the TLS and BLS (Kovács et al. 2002) periodograms to check if they present similar peaks. Next, to diminish the chances of the TLS detection being fortuitous, we randomly reshuffle the target light curve to remove the transiting signal and to simulate 1000 light curves with similar CDPP as the TFAW's frequency analysis step light curve. Using the batman package, we inject a transit signal with the parameters found by TLS. We run TLS over the simulated light curves and check whether the transit is recovered or not. If the transit is recovered in more than 90 per cent of the simulated light curves, then it passes to the final vetting step. We use the publicly available vespa[6] software (Morton 2012, 2015) to evaluate the FPP of our transit candidates. For each of the candidates, we supply the software with their corresponding TFAW phase-folded light curve, their celestial coordinates, the stellar parameters of their host star, and its photometry. We also compute a limiting aperture obtained from the validation sheets from the EVEREST 2.0 data base, and inspect independent photometry and high-angular resolution images to evaluate contamination from other sources. Using such information, vespa calculates the probabilities of the transiting signal being caused by non-associated blended eclipsing binaries, eclipsing binaries, hierarchical triples, and non-associated stars with transiting planets. Only candidates with an FPP lower than 1 per cent are considered as valid candidates.

4.3 Comparison with other searches

In Table 8, we show that our K2-C1 TFAW- and TLS-based planet search is able to recover all confirmed planets and most of the K2 candidates from previous studies compiled in NASA Exoplanet Archive. Generally, the missing ones are usually single-transit events, not suitable for periodic signal searching algorithms like TLS, multi-periodic systems for which the current TFAW version only reconstructs the signal for the most significant period (though the other planets in the system might have also been detected in the TLS periodogram but with lower SDEs), or some that present an SDE_{TLS} <9 (usually above 6.5) but have their most significant peak at the catalogued period. For the confirmed planets, TFAW finds at least one planet for each of the 35 catalogued planetary systems. For the ones in Barros, Demangeon & Deleuil (2016), TFAW detects 18 transiting systems, one with a period of >40 d is missed by TLS, and for another TLS does not find a significant peak at the listed period. For Crossfield et al. (2016), we detect 9 of the 13 listed candidates

[5]https://exoplanetarchive.ipac.caltech.edu

[6]https://github.com/timothydmorton/VESPA

Downloaded from https://academic.oup.com/mnras/article/498/2/2778/5894404 by guest on 10 November 2023

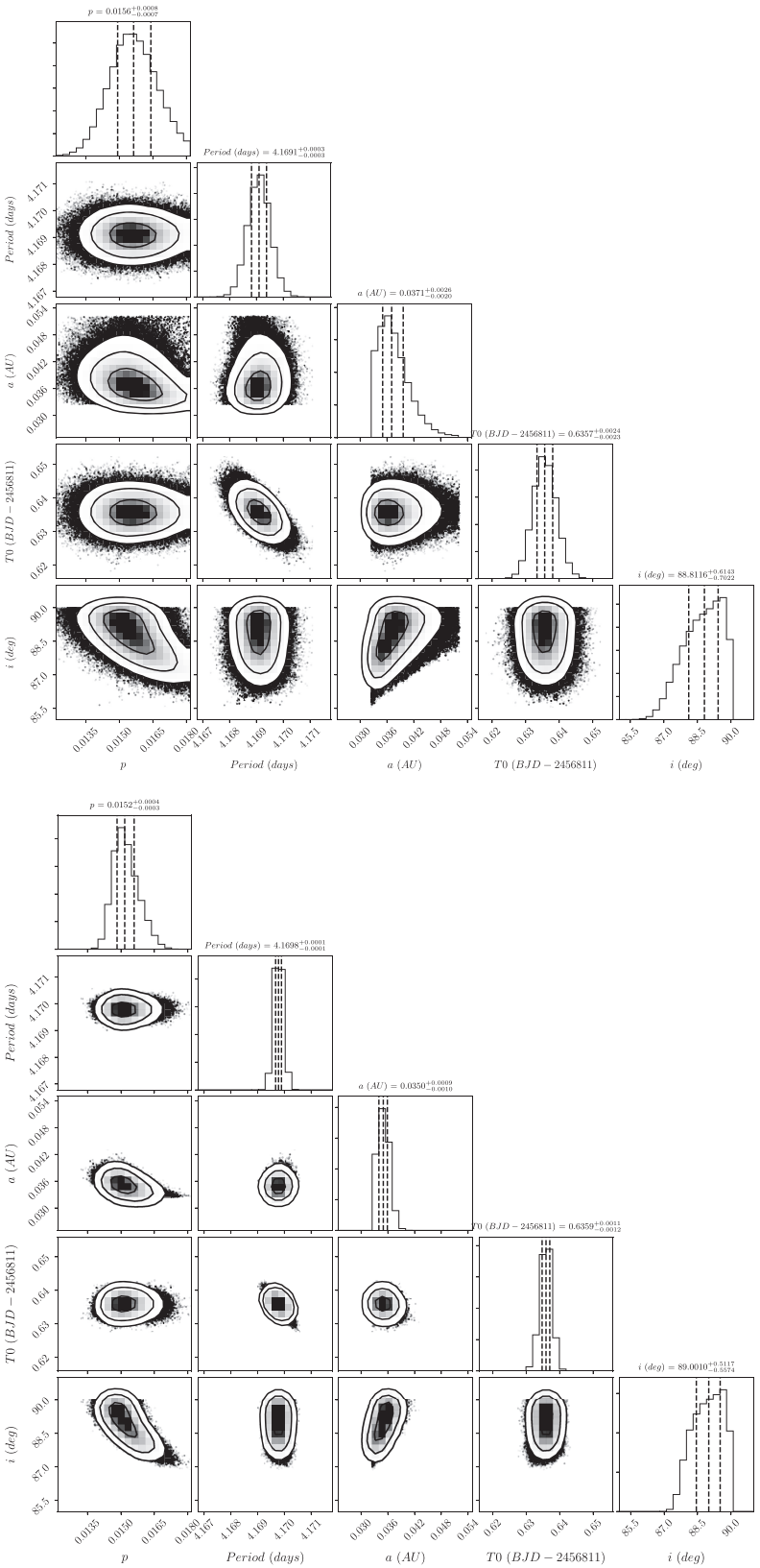

Figure 8. 1D and 2D projections of the posterior probability distributions of the five MCMC fitted parameters (p, P, a, T_0, and i) for K2-298 b `EVEREST 2.0` (top) and `TFAW` (bottom) detrended light curves. The 25, 50, and 75 per cent quantiles are displayed in dashed vertical lines on the 1D histograms and on the top each panel column.

Downloaded from https://academic.oup.com/mnras/article/498/2/2778/5894404 by guest on 10 November 2023

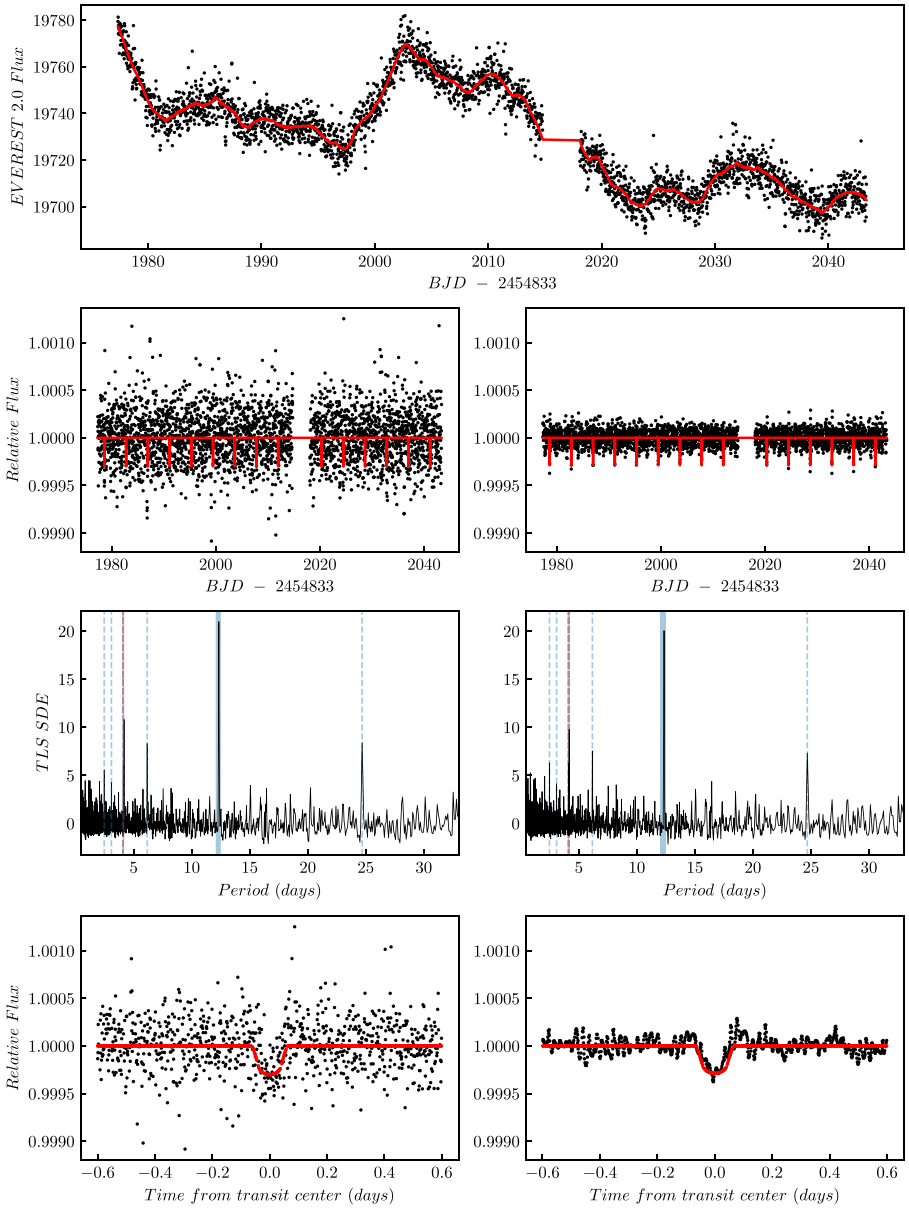

Figure 9. *From top to bottom*, the panels show the K2-298 raw flux of the EVEREST 2.0 light curve (with the running median in red), the entire light curve with in-transit data of the new candidate marked in red (left for EVEREST 2.0 and right for TFAW), the SDE_{TLS} periodogram (left for EVEREST 2.0 and right for TFAW), and the normalized phase-folded to the K2-298 b period light curve with MCMC fit data marked in red (left for EVEREST 2.0 and right for TFAW).

Table 8. Comparison of our planet search to previous groups, all subsampled to the K2-C1 campaign.

Candidate list	Catalogued planets	Number we found
Confirmed	48	35
Barros et al. (2016)	20	18
Crossfield et al. (2016)	13	9
Vanderburg et al. (2016)	72	68
Mayo et al. (2018)	13	13
Kruse et al. (2019)	97	78

for C1. Two of the missing ones are candidates with periods of >40 d; for the other two, TLS does not find a significant peak at the listed periods. Regarding Vanderburg et al. (2016), we detect 68 of the listed candidates. The other four are single transit or have a period of >40 d. We detect all the candidates for C1 listed by Mayo et al. (2018). Finally, we detect at least one planet in all 78 non-single-transit systems in Kruse et al. (2019). We believe that our new candidates presented here went undetected by other groups due to the combination of two factors, the increased photometric precision achieved with TFAW, specially for faint magnitudes, together with TLS improved capabilities to detect smaller planets.

4.4 Two new transit candidates from the K2-C1 data

In this section, we present two new transit candidates detected using the combination of the increased photometric precision of TFAW-corrected light curves and TLS. Both candidates have passed the vetting procedure explained in 4.2. As with K2-44 b and K2-298 b, once detected, we checked the EVEREST 2.0 light curves after masking the new candidate transits [given their smaller transit depths, the effect of the PLD can decrease the

Downloaded from https://academic.oup.com/mnras/article/498/2/2778/5894404 by guest on 10 November 2023

Table 9. Stellar parameters for EPIC 201170410 host star, TLS-detection parameters for the transit planetary candidate EPIC 201170410.02, TLS and vespa vetting parameters, and MCMC fit and derived planetary candidate parameters of EPIC 201170410.02.

K2 ID	EPIC 201170410
Stellar parameters	
Stellar radius R_s ($R_\odot$)	$0.282^{+0.074}_{-0.069}{}^{d}$
Stellar mass M_s ($M_\odot$)	$0.287^{+0.101}_{-0.084}{}^{d}$
Effective temperature (K)	$3648^{+172}_{-143}{}^{d}$
Surface gravity [$\log_{10}$(cm s^{-2})]	4.999 ± 0.075^{d}
Metallicity [Fe/H]	$-0.048^{+0.150}_{-0.210}{}^{d}$
Distance (pc)	$134.0^{+45.8}_{-39.8}{}^{d}$
Luminosity L_s ($L_\odot$)	–
Luminosity class	Dwarf^{e}
Spectral type	–
TLS-detection transit parameters	
Number of transits	10^{a}
Period P (days)	6.799 025
Epoch T_0 (BJD – 2454833) (days)	1980.14697625
Duration (hours)	1.849 331 04
Depth δ (per cent)	0.136
SNR	6.97^{c}
Radius ratio p	0.033 5913
Scaled semimajor axis a (au)	0.046 3297
Planetary radius R_p ($R_\oplus$)	1.033 2548
TLS and vespa vetting parameters	
SDE_{TLS}	9.382
ρ (arcsec)	22.5
FPP	4.8×10^{-10}
MCMC transit parameters	
Period P (days)	6.7987 ± 0.0001
Epoch T_0 (BJD – 2454833) (days)	$1980.1485^{+0.0006}_{-0.0005}$
Eccentricity e	0 (assumed)
Radius ratio p	$0.0340^{+0.0007}_{-0.0006}$
Scaled semimajor axis a (au)	$0.0349^{+0.0027}_{-0.0022}$
Inclination i (°)	$89.0025^{+0.4142}_{-0.2885}$
Derived planetary parameters	
Planetary radius R_p ($R_\oplus$)	$1.047^{+0.276}_{-0.257}{}^{b}$
Impact parameter b	$0.46^{+0.20}_{-0.14}{}^{b}$

Notes. [a]Denotes the number of transits detected by TLS that have data.
[b]Denotes values derived from fitted values.
[c]As defined in Pont, Zucker & Queloz (2006).
[d]Denotes values derived from Huber et al. (2016).
[e]Denotes values derived from Stassun et al. (2019).

Table 10. Stellar parameters for EPIC201757695 host star, TLS-detection parameters for the transit planetary candidate EPIC201757695.02, TLS and vespa vetting parameters, and MCMC fit and derived planetary candidate parameters of EPIC201757695.02.

K2 ID	EPIC 201757695
Stellar parameters	
Stellar radius R_s ($R_\odot$)	$0.655^{+0.041}_{-0.045}{}^{d}$
Stellar mass M_s ($M_\odot$)	$0.727^{+0.044}_{-0.053}{}^{d}$
Effective temperature (K)	$4520^{+108}_{-54}{}^{d}$
Surface gravity [$\log_{10}$(cm s^{-2})]	$4.659^{+0.035}_{-0.025}{}^{d}$
Metallicity [Fe/H]	$-0.003^{+0.120}_{-0.300}{}^{d}$
Distance (pc)	$577.6^{+33.2}_{-29.8}{}^{e}$
Luminosity L_s ($L_\odot$)	$0.433^{+0.482}_{-0.385}{}^{f}$
Luminosity class	Dwarf^{g}
Spectral Type	–
TLS-detection transit parameters	
Number of transits	30^{a}
Period P (days)	2.047 790 36
Epoch T_0 (BJD – 2454833) (days)	1978.6419269
Duration (hours)	1.822 56
Depth δ (per cent)	0.021
SNR	11.04^{c}
Radius ratio p	0.012 48
Scaled semimajor axis a (au)	0.028 3772
Planetary radius R_p ($R_\oplus$)	0.891 695
TLS and vespa vetting parameters	
SDE_{TLS}	15.005
ρ (arcsec)	18.3
FPP	8.13×10^{-5}
MCMC transit parameters	
Period P (days)	2.0478 ± 0.0001
Epoch T_0 (BJD – 2454833) (days)	$1978.6370^{+0.0008}_{-0.0007}$
Eccentricity e	0 (assumed)
Radius ratio p	0.0127 ± 0.0002
Scaled semimajor axis a (au)	0.0296 ± 0.0005
Inclination i (°)	$89.2757^{+0.3689}_{-0.3717}$
Derived planetary parameters	
Planetary radius R_p ($R_\oplus$)	$0.908\,19^{+0.058\,61}_{-0.064\,01}{}^{b}$
Impact parameter b	0.12 ± 0.06^{b}

Notes. [a]Denotes the number of transits detected by TLS that have data.
[b]Denotes values derived from fitted values.
[c]As defined in Pont et al. (2006).
[d]Denotes values derived from Huber et al. (2016).
[e]Denotes values derived from Bailer-Jones et al. (2018).
[f]Denotes values derived from Gaia Collaboration (2018).
[g]Denotes values derived from Stassun et al. (2019).

transit depth up to ∼10 per cent (Luger et al. 2018)]. Finally, in order to determine the transit parameters of these new candidates, we use the TFAW-corrected light curves, the TLS output, and the catalogued stellar properties as the starting point for the MCMC fit. As mentioned before, a complete study of observing campaign C1 (and C2-C18) is underway where more transit candidates are expected to be found. In Tables 9 and 10, we summarize the stellar and transit properties of the two new planetary candidates fully described in Sections 4.4.1 and 4.4.2.

4.4.1 EPIC 201170410

EPIC 201170410 is a $K_p = 15.673$ mag, $G = 16.4386$ mag (Gaia Collaboration 2018), $K_s = 12.619 \pm 0.027$ mag, and $(J - K_s) = 0.84 \pm 0.037$ (Skrutskie et al. 2006) star. It is located at (α, δ) = (11:20:33.81, −04:48:25.21) (Gaia Collaboration 2018) and observed by the K2 mission during the C1 monitoring campaign, channel 55.

Table 9 lists the catalogued stellar parameters by Huber et al. (2016) and Stassun et al. (2019) for this source. Gaia Collaboration (2018) provides a $T_{\rm eff} = 4013^{+714}_{-713}$ K, which is compatible within the previous listed value. This target is classified as a dwarf by Stassun et al. (2019) and, given its catalogued radius, mass, and effective temperature it is most likely an M-dwarf. No variability detection for this star is provided either in Armstrong et al. (2015, 2016), Watson et al. (2006), or Gaia Collaboration (2018).

Downloaded from https://academic.oup.com/mnras/article/498/2/2778/5894404 by guest on 10 November 2023

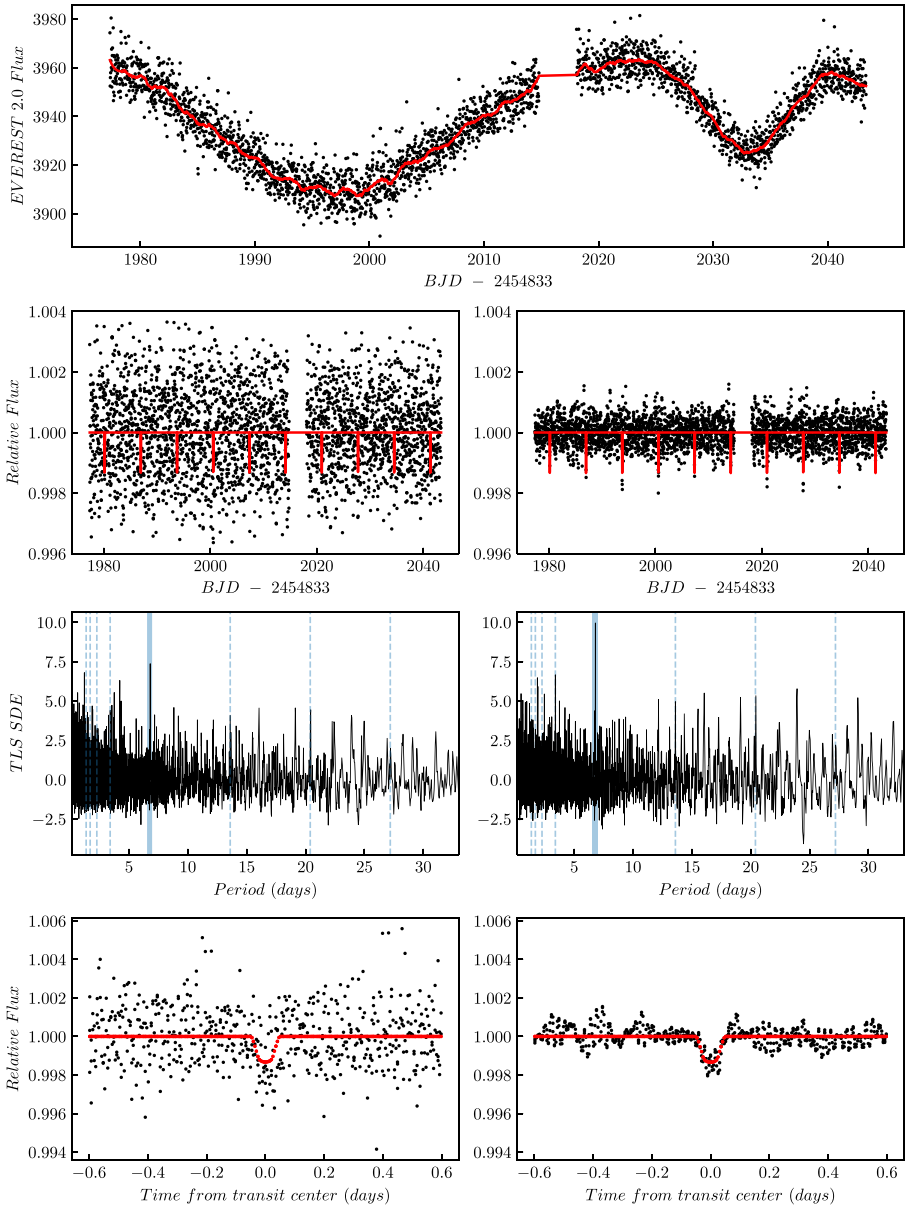

Figure 10. *From top to bottom*, the panels show the EPIC 201170410 raw flux of the EVEREST 2.0 light curve (with the running median in red), the entire light curve with in-transit data of the new candidate marked in red (left for EVEREST 2.0 and right for TFAW), the SDE_{TLS} periodogram (left for EVEREST 2.0 and right for TFAW), and the normalized phase-folded light curve with MCMC fit data marked in red (left for EVEREST 2.0 and right for TFAW).

Table 9 also summarizes the detection and vetting parameters obtained with TLS and vespa for the EPIC 201170410 TFAW-corrected light curve. With an SDE_{TLS}>9.0 and an FPP of 4.8×10^{-10}, it can be considered as a statistically validated exoplanet candidate (Heller et al. 2019). Finally, it also lists the transit and derived planetary parameters obtained from the MCMC fit of the TFAW-corrected light curve.

Fig. 10 shows the summary plot displaying the PLD, CBV-corrected flux provided by the EVEREST 2.0 pipeline for EPIC 201170410 with the 2-d running median plotted in red, the EVEREST 2.0 median-filtered light curve and the TFAW-corrected light curves (with the MCMC-derived transit data of the new candidate plotted in red), the TLS periodograms for EVEREST 2.0 and TFAW's frequency analysis step, and the phase-folded lights curve with the MCMC fit data (red line) for EVEREST 2.0 (left) and TFAW iteratively denoised and reconstructed one (right). The TLS periodograms show the position of the candidate's detected period (solid blue line) and its harmonics (dashed blue lines).

As can be seen from the TLS periodograms, the peak at 6.7987 d is visible for both EVEREST 2.0 and TFAW. However, for the latter, and given TFAW's denoising capabilities, this peak has a higher SDE_{TLS} (9.4 versus 7.4) that allows it to cross our significant detection threshold (i.e. >9). In the particular case of EVEREST 2.0-detrended light curve, EPIC 201170410.02 might not have been detected by other authors, even those using TLS, because the light-curve noise sets the SDE_{TLS} below the detection threshold employed by them [9.0 in the case of Hippke & Heller (2019) and Heller et al. (2019)]. In addition, the transit-like feature becomes clearly visible in the reconstructed TFAW light curve (the right plot in the second row in Fig. 10 and the right bottom plot in Fig. 10). It is worth mentioning

Downloaded from https://academic.oup.com/mnras/article/498/2/2778/5894404 by guest on 10 November 2023

that the wavelet does not have an a priori knowledge of the shape of the underlying signal in a given light curve and that its shape is estimated only from the phase-folded light curve at a given period and is re-estimated at every iteration step during TFAW's signal reconstruction step. As shown in Section 3.5.4 with K2-298 b, EPIC 201170410 shows another example of the potential of TFAW to detect and recover transit-like features even for highly noisy light curves as this one.

To confirm that our candidate light curve was not affected by contamination of nearby sources, we visually inspect the K2-C1, channel 55, calibrated full frame images (FFIs) for EPIC 201170410. In addition, Gaia Collaboration (2018) does not list any other source within EPIC 201170410 aperture either. As explained in Section 4.2, using EVEREST 2.0 validation sheets for EPIC 201170410 we assigned the maximum aperture radius for vespa, $\rho = 22.5$ arcsec, to estimate the possibility of contamination by other objects.

EPIC 201170410 has also been observed by the *TESS* mission in Sector 9 (2019 28 February to 26 March). EPIC 201170410 corresponds to TIC 38116202. However, no light curve for this target is available from the usual *TESS* data archives. We download the *TESS* FFI corresponding to TIC 38116202 using the eleanor[7] package and use it to compute raw, CBV-corrected and PSF-modelled light curves for this target. TIC 38116202 is highly affected by crowding from two other near and brighter stars in the TESS FFI leading to a worse photometric solution than the one from K2; thus, no conclusive results can be obtained from this light curve after running the period search using TLS.

Finally, in order to better determine the EPIC 201170410.02 transit and planetary parameters, we run an MCMC fit over the TFAW-corrected light curve using the TLS output as initial guess values. Table 9 lists the obtained MCMC fit and planetary derived values. For EPIC 201170410.02, assuming a circular orbit, TFAW yields a $1.047^{+0.276}_{-0.257}\mathrm{R}_\oplus$ planet orbiting its host star at $0.0349^{+0.0027}_{-0.0022}$ au with a period of 6.7987 ± 0.0001 d. With this radius value, EPIC 201170410.02 is the 10th smallest K2-C1 planet within those candidates with an estimated planetary radius and the 44th smallest in all K2 campaigns.

4.4.2 EPIC 201757695

EPIC 201757695 is a $K_\mathrm{p} = 14.599$ mag, $G = 14.6206$ mag (Gaia Collaboration 2018), $K_s = 12.149 \pm 0.026$ mag, $(J - K_s) = 0.707 \pm 0.037$ (Skrutskie et al. 2006) star. It is located at $(\alpha, \delta) = (11{:}35{:}45.24, +04{:}36{:}59.21)$ (Gaia Collaboration 2018) and observed by the K2 mission during the C1 monitoring campaign, channel 47.

Table 10 lists the catalogued stellar parameters by Huber et al. (2016), Bailer-Jones et al. (2018), Gaia Collaboration (2018), and Stassun et al. (2019) for this source. In addition, Gaia Collaboration (2018) provides a $T_\mathrm{eff} = 4706^{+290}_{-264}$ K, which is compatible within the previous listed value. This star is classified as a dwarf (Stassun et al. 2019) and, given its catalogued radius, mass, and effective temperature, it is most likely a K-type star. No variability detection for this star is provided either in Armstrong et al. (2015, 2016) or Gaia Collaboration (2018). It is catalogued as a 'variable star of unspecified type' (VAR) by the AAVSO International Variable Star Index (VSX)[8] (Watson et al. 2006) with a period of 19.940 41 d.

Table 10 also lists the detection and vetting parameters obtained with the TLS and vespa for the EPIC 201757695 TFAW-corrected light curve. With an $\mathrm{SDE_{TLS}} > 9$ and an FPP of 8.13×10^{-5}, EPIC 201757695.02 can be considered as a statistically validated exoplanet candidate. Finally, Table 10 also summarizes the transit and derived planetary parameters obtained from the MCMC fit of the TFAW-corrected light curve.

Fig. 11 shows the summary plot displaying the PLD, CBV-corrected flux provided by the EVEREST 2.0 pipeline for EPIC 201757695 with the 2-d running median plotted in red, the EVEREST 2.0 median-filtered light curve and the TFAW-corrected light curves (with the MCMC-derived transit data of the new candidate plotted in red), the TLS periodograms for EVEREST 2.0 and TFAW's frequency analysis step, and the phase-folded light curves with the MCMC fit data (red line) for EVEREST 2.0 (left) and TFAW iteratively denoised and reconstructed one (right). The TLS periodograms show the position of the candidate's detected period (solid blue line) and its harmonics (dashed blue lines).

The TLS periodograms in Fig. 11 show a clear peak at 2.048 d and with enough $\mathrm{SDE_{TLS}}$ to cross our detection threshold for both EVEREST 2.0 and TFAW. However, for the latter, again due to TFAW denoising capabilities, this significance is higher (15.0 versus 14.2). As with the case of EPIC 201170410, for EPIC 201757695 the transit feature becomes clearly more visible in the TFAW-corrected light curve.

To confirm that this second candidate was not affected by contamination from nearby sources, we visually inspect the K2-calibrated FFIs for EPIC 201757695. In addition, Gaia Collaboration (2018) does not show any other source within EPIC 201757695 aperture. Using EVEREST 2.0 validation sheets for this target, we assigned the maximum aperture radius for vespa, $\rho = 18.3$ arcsec as listed in Table 10.

EPIC 201757695 is included in the *TESS* Input Catalog (Stassun et al. 2019) as TIC 903075188. However, to date 2020 March 31, it has not been observed yet and no light curve is available for this target.

Again, in order to better determine EPIC 201757695.02 transit and planetary parameters, we run an MCMC fit over this target TFAW-corrected light curve using the TLS output as initial guess values.

Table 10 lists the obtained MCMC fit and planetary derived values. For EPIC 201757695.02, assuming a circular orbit, TFAW yields a $0.908^{+0.059}_{-0.064}\mathrm{R}_\oplus$ planet orbiting its host star at a distance of 0.0296 ± 0.0005 au with a period of 2.0478 ± 0.0001 d. With this radius value, EPIC 201757695.02 is the 9th smallest K2-C1 of the candidates with an estimated planetary radius, and the 39th smallest in all K2 campaigns.

5 CONCLUSIONS

We present the results obtained after applying the wavelet-based TFAW to further extend the photometric precision achieved by EVEREST 2.0 light curves from the K2 mission. We compare the photometric precision of both algorithms in terms of the 6 h CDPP. On average, the TFAW median 6 h CDPP is ∼30 per cent better than the one from EVEREST 2.0. This improvement can reach about ∼35–40 per cent in the faint magnitude range during TFAW's frequency analysis step. The 6 h CDPP of TFAW iteratively reconstructed and denoised light curves (i.e. those that have crossed the signal detection threshold) can be ∼50–75 per cent better than the corresponding EVEREST 2.0 one. We show that the transit detection efficiency of simulated Earth–Sun-like systems along the $8 < K_\mathrm{p} < 18$ mag range for TFAW is a factor of ∼8.5× on average higher than that for the case of EVEREST 2.0 light curves. This improvement

[7] https://github.com/afeinstein20/eleanor
[8] https://www.aavso.org/vsx/index.php

Downloaded from https://academic.oup.com/mnras/article/498/2/2778/5894404 by guest on 10 November 2023

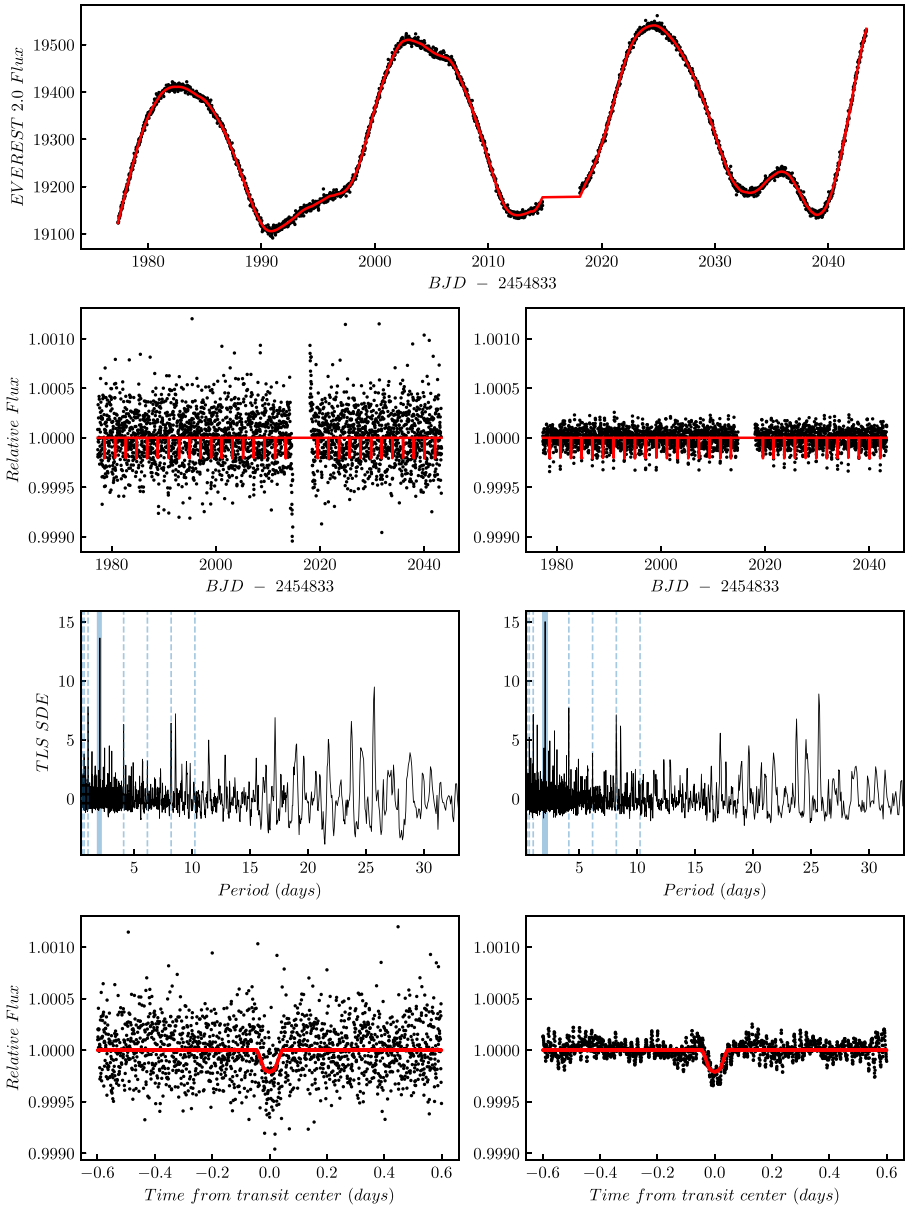

Figure 11. *From top to bottom*, the panels show the EPIC 201757695 raw flux of the EVEREST 2.0 light curve (with the running median in red), the entire light curve with in-transit data of the new candidate marked in red (left for EVEREST 2.0 and right for TFAW), the SDE_{TLS} periodogram (left for EVEREST 2.0 and right for TFAW), and the normalized phase-folded light curve with MCMC fit data marked in red (left for EVEREST 2.0 and right for TFAW).

increases up to ∼21× for the faint ($K_p > 15.0$) magnitude range. We validate our algorithm by performing transit injection/recovery tests where the planetary radius-to-stellar radius ratios (i.e. transit depths) are recovered without significant bias in the TFAW-corrected light curves.

We demonstrate that the TFAW-corrected light curves of two confirmed exoplanets, K2-44 b and K2-298 b, with high and low SNRs, yield better MCMC posterior distributions thanks to the lower noise contribution. In addition, TFAW yields transit parameters compatible with the catalogued ones but returns smaller uncertainties and narrows the credibility intervals. The TFAW improvement in the photometric performance, transit detection efficiency, and planetary characterization over the K2 data can be translated to other running missions, such as *TESS* and *CHEOPS* (Broeg et al. 2013).

We report the discovery of two statistically validated Earth-sized planets around dwarf stars, EPIC 201170410 and EPIC 201757695, using TFAW-corrected light curves from the EVEREST 2.0 data base for K2 observing campaign 1. While their small transit depths might not have been detectable and correctly characterized by other algorithms, the combination of the increased photometric precision achieved with TFAW, together with TLS improved capabilities to detect smaller planets, identified them as transit candidates. We use a rigorous vetting procedure, the vespa software, the EVEREST 2.0 validation, independent photometry, and high-angular resolution images to statistically validate these candidates. The MCMC characterization of the TFAW-corrected light curves of these candidates reveals that EPIC 201170410.02 is the 10th smallest planet in K2-C1 and the 44th in all K2 campaigns, whereas EPIC 201757695.02 is the 9th smallest candidate in K2-C1 and the 39th

Downloaded from https://academic.oup.com/mnras/article/498/2/2778/5894404 by guest on 10 November 2023

of all the K2 mission candidates. Work is still in progress to fully automate the vetting and FPP computation. A full list of statistically validated candidates for K2-C1 and all other K2 observing campaigns will be presented in a forthcoming paper.

ACKNOWLEDGEMENTS

This research has made use of the NASA Exoplanet Archive, which is operated by the California Institute of Technology, under contract with the National Aeronautics and Space Administration under the Exoplanet Exploration Program. This work made use of NASA ADS Bibliographic Services. This research has made use of `Aladin` sky atlas developed at CDS, Strasbourg Observatory, France. This work has made use of data from the European Space Agency (ESA) mission *Gaia*. DdS acknowledges funding support from the Reial Acadèmia de Ciències i Arts de Barcelona (RACAB). DdS and OF also acknowledge support by the Spanish Ministerio de Economía, Industria y Competitividad (MINEICO/FEDER, UE) under grants AYA2016-76012-C3-1-P, PID2019-105510GB-C31, and MDM-2014-0369 of ICCUB (Unidad de Excelencia 'María de Maeztu').

DATA AVAILABILITY

The data underlying this article will be shared on reasonable request to the corresponding author.

REFERENCES

Akeson R. L. et al., 2013, PASP, 125, 989
Ambikasaran S., Foreman-Mackey D., Greengard L., Hogg D. W., O'Neil M., 2015, IEEE Trans. Pattern Anal. Mach. Intell., 38, 252
Andrae R. et al., 2018, A&A, 616, A8
Armstrong D. J. et al., 2015, A&A, 579, A19
Armstrong D. J. et al., 2016, MNRAS, 456, 2260
Bailer-Jones C. A. L., Rybizki J., Fouesneau M., Mantelet G., Andrae R., 2018, AJ, 156, 58
Barros S. C. C., Demangeon O., Deleuil M., 2016, A&A, 594, A100
Bernardo J., Berger J. O., Dawid A. P., Smith A. F. M., 1996, Bayesian Statistics 5: Proc. Fifth Valencia Int. Meeting, June 5–9, 1994, Valencia International Meeting on Bayesian Statistics, Vol. 5. Oxford Science Publications, Clarendon Press, Oxford
Broeg C. et al., 2013, in Roberto S., ed., EPJ Web Conf., Vol. 47, Hot Planets and Cool Stars. EDP Sci., Les Ulis Cedex A, France, p. 03005
Chakrabarty A., Sengupta S., 2019, AJ, 158, 39
Christiansen J. L. et al., 2012, PASP, 124, 1279
Claret A., 2018, A&A, 618, A20
Crossfield I. J. M. et al., 2016, ApJS, 226, 7
del Ser D., Fors O., Núñez J., 2018, A&A, 619, A86
Deming D. et al., 2015, ApJ, 805, 132
Foreman-Mackey D., 2016, J. Open Source Softw., 1, 24
Foreman-Mackey D., Hogg D. W., Lang D., Goodman J., 2013, PASP, 125, 306
Gaia Collaboration, 2018, A&A, 616, A1
Goossens B., Pizurica A., Philips W., 2009, IEEE Transactions on Image Processing, 18, 1153
Heller R., Hippke M., Rodenbeck K., 2019, A&A, 627, A66
Hippke M., Heller R., 2019, A&A, 623, A39
Howell S. B. et al., 2014, PASP, 126, 398
Huber D. et al., 2016, ApJS, 224, 2
Jansen M., Bultheel A., 1999, IEEE Trans. Image Process., 8, 947
Kostov V. B. et al., 2019, AJ, 157, 124
Kovács G., Zucker S., Mazeh T., 2002, A&A, 391, 369
Kovács G., Bakos G., Noyes R. W., 2005, MNRAS, 356, 557
Kreidberg L., 2015, PASP, 127, 1161
Kruse E., Agol E., Luger R., Foreman-Mackey D., 2019, ApJS, 244, 11
Luger R., Agol E., Kruse E., Barnes R., Becker A., Foreman-Mackey D., Deming D., 2016, AJ, 152, 100
Luger R., Kruse E., Foreman-Mackey D., Agol E., Saunders N., 2018, AJ, 156, 99
Lund M. N., Handberg R., Davies G. R., Chaplin W. J., Jones C. D., 2015, ApJ, 806, 30
Mandel K., Agol E., 2002, ApJ, 580, L171
Mayo A. W. et al., 2018, AJ, 155, 136
Montet B. T. et al., 2015, ApJ, 809, 25
Morton T. D., 2012, ApJ, 761, 6
Morton T. D., 2015, VESPA: False Positive Probabilities Calculator, Astrophysics Source Code Library, record ascl:1503.011
Pont F., Zucker S., Queloz D., 2006, MNRAS, 373, 231
Ricker G. R. et al., 2015, J. Astron. Telesc. Instrum. Syst., 1, 014003
Sing D. K., 2010, A&A, 510, A21
Skrutskie M. F. et al., 2006, AJ, 131, 1163
Stassun K. G. et al., 2019, AJ, 158, 138
Stetson P. B., 1996, PASP, 108, 851
Vanderburg A., Johnson J. A., 2014, PASP, 126, 948
Vanderburg A. et al., 2016, ApJS, 222, 14
Watson C. L., Henden A. A., Price A., 2006, Soc. Astron. Sci. Annu. Symp., 25, 47
Zacharias N., Finch C. T., Girard T. M., Henden A., Bartlett J. L., Monet D. G., Zacharias M. I., 2013, AJ, 145, 44
Zink J. K., Hardegree-Ullman K. K., Christiansen J. L., Dressing C. D., Crossfield I. J. M., Petigura E. A., Schlieder J. E., Ciardi D. R., 2020, AJ, 159, 154

This paper has been typeset from a TEX/LATEX file prepared by the author.

Downloaded from https://academic.oup.com/mnras/article/498/2/2778/5894404 by guest on 10 November 2023